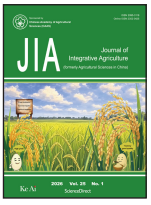
Journal of Integrative Agriculture 2026, 25(1): 207–226

Available online at ScienceDirect

Journal of Integrative Agriculture



RESEARCH ARTICLE

3D genomic alterations during development of skeletal muscle in chicken

Zhongxian Xu[1, 2, 3*], Tao Wang[2, 3*], Wei Zhu[2*], Maosen Yang[2], Dong Leng[2], Ziyu Li[2], Jiaman Zhang[2], Pengliang Liu[2], Zhoulin Wu[4], Mengnan He[5], Yan Li[5], Hua Kui[2], Xue Bai[2], Bo Zeng[2], Yao Zhang[2], Qing Zhu[2], Xiaoling Zhao[2], Mingzhou Li[2#], Diyan Li[2, 3#]

[1] *Key Laboratory of Southwest China Wildlife Resources Conservation (Ministry of Education), China West Normal University, Nanchong 637009, China*
[2] *Institute of Animal Genetics and Breeding, College of Animal Science and Technology, Sichuan Agricultural University, Chengdu 611130, China*
[3] *Antibiotics Research and Re-evaluation Key Laboratory of Sichuan Province, Sichuan Industrial Institute of Antibiotics, School of Pharmacy, Chengdu University, Chengdu 610106, China*
[4] *Key Laboratory of Meat Processing of Sichuan, College of Food and Biological Engineering, Chengdu University, Chengdu 610106, China*
[5] *Chengdu Research Base of Giant Panda Breeding, Chengdu 611081, China*

Highlights

- Multi-stage 3D genomic and epigenomic maps reveal dynamic chromatin reorganization during chicken muscle development.
- A/B compartment switching and TAD remodeling are tightly linked to transcriptional transitions from myogenesis to aging.
- Promoter-enhancer rewiring underlies stage-specific activation of muscle growth and senescence-associated genes.

Abstract

The development of skeletal muscle are complicated processes involving genes responsible for proper muscle morphology, contractility, cell proliferation, differentiation, interactions, migration, and death. The three-dimensional chromatin architecture of skeletal muscle development has not been studied intensively although dynamic transcriptional regulation during differentiation of muscle cells is one of the most deeply studied processes. The RNA-seq was used to analyze the transcriptome pattern during chicken muscle development across 12 stages. Hi-C was used to build chromatin architectures during four representative stages. ChIP-seq was conducted to identify enhancers and promoters in these four stages, which are occupied by histone H3K27ac and H3K4me3 peaks. Results show that large-scale genome architecture changes are mostly unidirectional, and coupled by complex on/off dynamic patterns of gene expression. Specifically, we observed 258.30 Mb of the genome undergoing A/B compartment switching. Notable alterations (316.57 Mb) of interaction frequencies within TADs were observed. Substantial aging-associated genes exhibited ascending connectivity with the compartment transition from repressive to active status during muscle development. Some muscle-related gene promoters that interacted with active enhancers during development, and some myopathy/aging-associated genes that were activated in aging muscle were founded. These results provide key insights into skeletal muscle development *in vivo*, and offer a valuable resource that allows in-depth functional characterization of candidate genes.

Keywords: skeletal muscle, development, gene expression, chromatin architecture

1. Introduction

Skeletal muscles (one of the three types of muscles in the animal body) account for about 35% of body mass (Luo *et al.* 2021), and are responsible for body movements and posture, maintenance, protection of internal organs and tissues, and regulation of body temperature. Aging is accompanied with muscle strength reduction by 30–40%, and can have catastrophic effects on the quality of life (Newman *et al.* 2006). Skeletal muscle development consists of prenatal myogenesis and postnatal hypertrophy of myofibers, and

Received 8 October 2023; Received in revised form 7 December 2023; Accepted 1 February 2024; Available online 16 March 2024
Zhongxian Xu, E-mail: xu_zhongxian@cwnu.edu.cn; Tao Wang, E-mail: wanttao@hotmail.com; Wei Zhu, E-mail: 1424518023@qq.com; #Correspondence Diyan Li, E-mail: lidiyan@cdu.edu.cn; Mingzhou Li, E-mail: mingzhou.li@sicau.edu.cn
*These authors contributed equally to this study.

© 2026 CAAS. Publishing services by Elsevier B.V. on behalf of KeAi Communications Co. Ltd. This is an open access article under the CC BY-NC-ND license (http://creativecommons.org/licenses/by-nc-nd/4.0/). Peer review under responsibility of Editorial Board of *Journal of Integrative Agriculture*.
doi: 10.1016/j.jia.2024.03.052

is orchestrated by a temporally dynamic interplay between gene regulatory networks and genome topology (Kocamis *et al.* 2001). The former process involves two successive waves of myofiber formation corresponding to the embryonic and fetal periods. The latter is typically characterized by the hypertrophy of fibers and by the functional maintenance and homeostasis of mature muscles (Berti *et al.* 2015). Early landmarks in skeletal muscle research focused primarily on protein-coding genes (Parker *et al.* 2003). However, in recent years another theme of keen interest is the identification of novel regulatory regions (non-coding) of the genome (Martone *et al.* 2019). The assignation of myogenic identity to the muscle progenitors is executed by organizing hierarchical interactions between transcriptional regulators, regulatory RNAs, and chromatin-remodeling factors (Bentzinger *et al.* 2012).

Most recently, remarkable achievements have been made to further elucidate the hierarchical package of nuclear chromatin by using Hi-C to investigate the 3D chromatin organization, including chromosome territories, compartments, TADs, and chromatin loops (Zheng and Xie 2019). This has been instrumental in unravelling the molecular basis of the chromatin architecture underlying crucial developmental events such as gametogenesis (Hammoud *et al.* 2014; Flyamer *et al.* 2017), lineage commitment, stem cell differentiation (Dixon *et al.* 2015; Paulsen *et al.* 2019), and embryonic development (Ljt *et al.* 2018). The activation of *Hox* genes is temporally dynamic in embryonic development. These genes are initially organized as single tightly packed and inactive chromatin compartments that become relaxed and switched on as the embryo develops (Noordermeer *et al.* 2014). Furthermore, *Hoxd1–Hoxd10* are exclusively manipulated in the initial phase of limb bud formation by enhancers located in the 3′ TAD, and *Hoxd11–Hoxd13* are subsequently activated by enhancers in the 5′ TAD (Deschamps and Duboule 2017). TADs have significant enrichment for myogenic-specific genes (Neems *et al.* 2016). As an example, the activation of embryonic myogenesis requires a sub-TAD-affected, long-range chromatin interaction between *Pax3* and *Ldb1* (Magli *et al.* 2019). The *Shh* locus TAD facilitates distance-independent contacts and enables functional communication with the distal ZRS enhancer (Symmons *et al.* 2016), which can be explained by the looping model for enhancer-promoter communication. As a trigger of transcription, enhancer-promoter pairing like ZRS-Shh and Pen-Pitx1 interactions mediate on/off switching of gene expression during limb development (Kragesteen *et al.* 2018; Paliou *et al.* 2019). New interactions of the limb enhancer Epha4 (also located in a large TAD) have been shown to interact with *Wnt6*, *Ihh*, and *Pax3* located in two smaller flanking TADs (Lupianez *et al.* 2015).

Recognized as a key hallmark of aging, senescence also plays a vital role in tissue patterning during development, including wound healing and tissue repair (Chandra *et al.* 2015; Criscione *et al.* 2016). Although dramatic changes have been confirmed in the chromatin landscape at different levels of organization in senescent cells (Chandra *et al.* 2015; Sati *et al.* 2020), there is a remaining challenge in the field of muscle aging.

The limited understanding of mechanisms between genome topology and skeletal muscle development prompted us to investigate the intricate regulatory orchestration of gene expression in this area. How chromatin organization facilitates vital gene expression programs, and temporally sets the epigenetic state remains unknown. Additionally, despite the vast amount of research into age-related changes in skeletal muscle, the mechanisms involved are poorly understood, and treatments to preserve muscle function with aging remain elusive. To explore the dynamic characters of 3D genome architecture and the contributions to transcriptional regulation during chicken skeletal muscle development, we have systematically depicted the dynamic transcriptomic profiles of pectoral muscle collected from 12 representative developmental stages covering (1) five embryonic stages of myogenesis: embryonic days 9 (E9), 12 (E12), 15 (E15), 18 (E18), and 20 (E20), (2) four postnatal stages of muscle growth: days 1 (D1), 36 (D36), 100 (D100), and 300 (D300), and (3) three postnatal stages of muscle homeostasis maintenance: years 3 (Y3), 5 (Y5), and 8 (Y8) (Fig. 1-A). We found 258.30 Mb of switched compartments, 316.57 Mb of alteration intra-TADs, and 33.15% dynamic interactions of promoter-enhancer pairing during muscle embryogenesis, development, and senescence. Together, our observations indicate that the dynamic genome architecture can facilitate the transcription of muscle-related genes in developing chickens.

2. Materials and methods

2.1. Animals and tissue collection

Fertile eggs (Chinese native Tibetan chicken) were purchased from Mao County Jiuding Original Ecological Livestock and Poultry Breeding Co., Ltd., Aba Autonomous Prefecture, Sichuan Province, China. Chicken embryo incubation and chick raising were conducted at the Avian Farm of Sichuan Agricultural University, China. All administrations and embryonic sex determination were carried out as previously described (Xu *et al.* 2018). Female chickens were euthanized at the major developmental stages described in previous sections, pectoral muscles were collected and flash frozen in liquid nitrogen and stored at –80°C for subsequent assays. Fresh muscle tissue was fixed in 10% formalin for histological analysis.

2.2. Histology analysis

Samples were fixed in 10% formalin in PBS, paraffin embedded, sectioned, and stained with haematoxylin and eosin before image analysis. In each sample image, 200 clearly delineated muscle fibers were selected to measure the diameter and cross section area. To eliminate the bias introduced by incomplete transection of muscle fibers, we selected measurements at locations with shorter diameter, and removed 50 each of the largest and smallest measurements to perform statistical analysis of the diameter and cross-sectional area. We also counted the number of muscle cell in 10 muscle bundles and conducted multiple comparisons in order to exhibit the increase of muscle cell numbers during the secondary fiber formation (E12, E15, E18

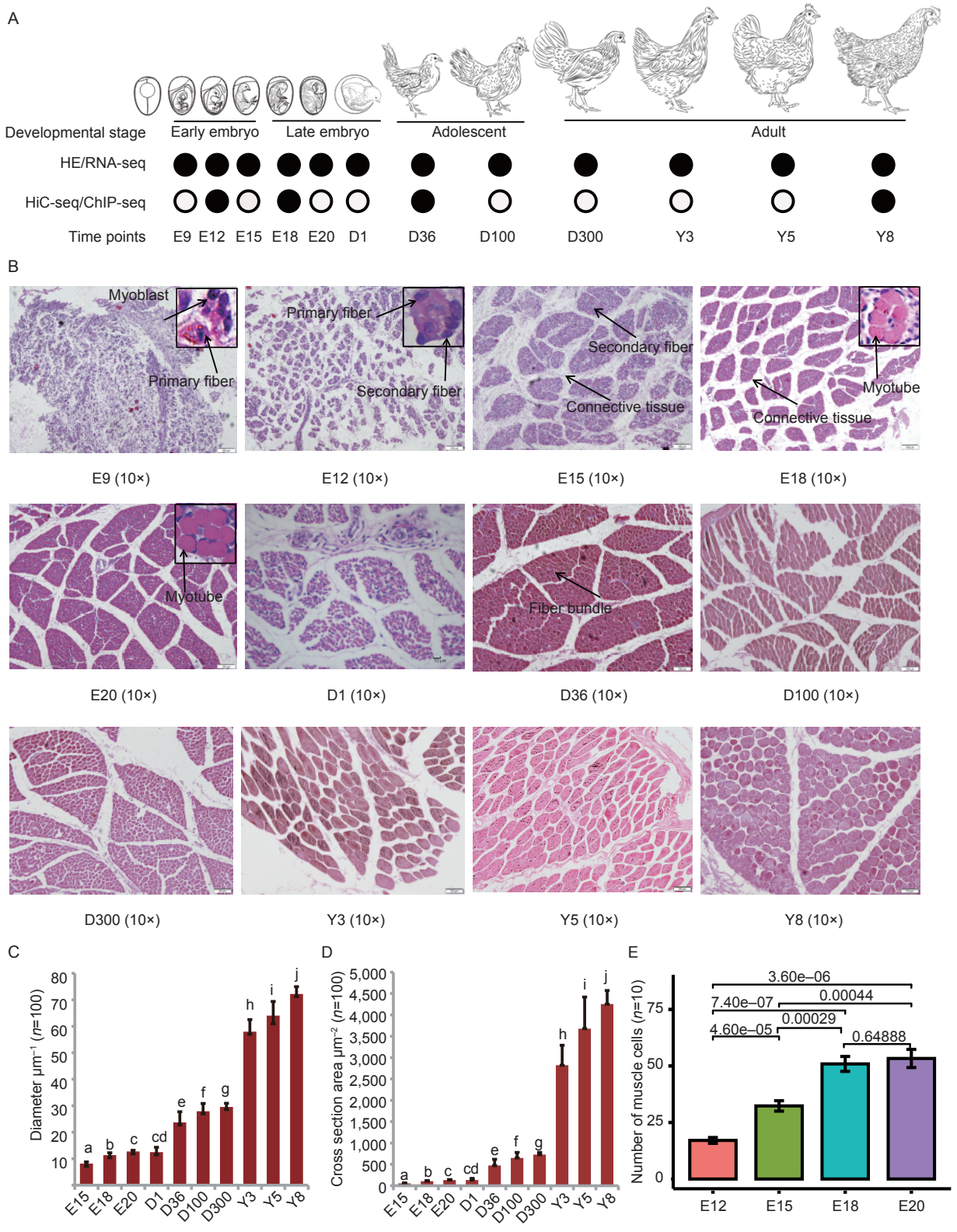


Fig. 1 Skeletal muscle developmental morphological characteristics. A, developmental stage sampled and multi-omics data sequenced in chicken skeletal muscle (pectoral muscle). In total, 4 stages across 12-time points were sampled, including the early embryo (E9, E12, and E15), the late embryo (E18, E20, and D1), the adolescent (D36 and D100), and the adult (D300, Y3, Y5, and Y8) stages. RNA-seq analysis was performed (in duplicate or triplicate) for all 12 developmental stages. Hi-C and ChIP-seq experiments were performed in duplicate at the following four typical developmental stages: primary myofiber formation (E12); secondary myofiber formation (E18); critical period of muscle development (D36); and aging phase (Y8). B, histological section of skeletal muscle at 12 developmental stages. Scale bar=100 μm. C, myofibre diameter. D, cross-sectional area. Duncan's multiple comparison method was performed. Bar plots with different letters indicate differential significance (P<0.05), the same letters mean non-significant difference. E, the number of muscle cells in embryonic stages. P-values were calculated using the t-test. Data are mean±SD.

and E20). The variance was determined by one-way ANOVA in R, and multiple comparisons were applied to conduct Duncan's test for 10 time points.

2.3. Total RNA-seq and data analysis

Total RNA was extracted from duplicates (for D1, D300, Y5 and Y8) or triplicates for all other time points using the Qiagen RNeasy Kit (Qiagen, Germany). Ribosomal RNA (rRNA) was removed with the Epicentre *Ribo-Zero*™ rRNA Removal Kit (Epicentre, USA) following the manufacturer's protocol. A total of 32 libraries were constructed, and paired-end sequencing (2×150 bp) was performed on the Illumina Hiseq 2500 platform (Annoroad, Beijing).

The processed high-quality reads were mapped to the chicken reference genome using TopHat2 (Kim *et al.* 2013), the aligned reads were assembled using StringTie v1.3.3, and transcripts were constructed using Cufflinks 2.0.2 software (Pertea *et al.* 2015; Ghosh and Chan 2016). Candidate transcripts were categorized as protein-coding genes (PCGs, with coding potential). The expression levels of the transcripts were quantified as transcripts per million (TPM) values using StringTie. Transcripts with TPM≥0.5 in at least two biological replicates were denoted as expressed PCGs. Next, transcriptome complexity analysis was conducted as described in (Mele *et al.* 2015). Developmentally dynamic genes (DDGs) were identified using maSigPro (microarray significant profiles) (Nueda *et al.* 2014). Differentially expressed PCGs were further identified using DESeq2 (Love *et al.* 2014). Using a FDR<0.01 and $|\log_2(\text{fold change})|>2$ as the threshold, the obtained 2,366 DDGs were classified as distinct clusters with characteristic expression patterns and dynamics by applying the *k*-means with $R^2>0.6$ and $P<0.001$. DDGs in consecutive stages of pre- and post-natal were determined by Short Time-series Expression Miner (STEM, v1.3.13). Metascape was used to determine the gene ontology enrichments of each cluster (Cardoso-Moreira *et al.* 2019; Zhou *et al.* 2019).

2.4. ChIP-seq and data analysis

Chromatin immunoprecipitation was performed as follows. Briefly, the cell nuclear suspension obtained from homogenized fresh muscle tissues were resuspended in cold cell lysis buffer (10 mmol L^{-1} Tris, pH 8, 10 mmol L^{-1} NaCl, 0.2% NP-40). Cross-linking was performed on samples of 1×10^7 cells with formaldehyde and glycine. These were next centrifuged for 5 min at 1,000×g, and the pellets were resuspended in ChIP lysis buffer (750 μL per 1×10^7 cells). Sonication was performed in a Bioruptor (Diagenode, Belgium) to yield ~200 bp fragments. The supernatant was diluted in RIPA buffer, and an antibody specific to H3K4me3/H3K27ac was added into 25 ug prepared DNA per IP. An equal volume of protein A and protein G beads were added, and incubation was conducted overnight at 4°C. Antibody-bound DNA was washed four times in RIPA buffer, and ChIPed DNA was reverse-crosslinked and purified for library construction following the Illumina ChIP-seq library generation protocol. Finally, the samples were sequenced on Illumina NextSeq500 or HiSeq X Ten (Annoroad, Beijing).

Trimmed raw reads preprocessed by FastQC and Trim Galore were aligned to the Gallus_gallus6.0 using Bowtie2 v2.2.5 (Langmead and Salzberg 2012). Duplicates were removed using Picard v1.90, and aligned reads were made from the non-redundant fraction (NRF). Antibody enriched domains (peak calling) were identified with MACS2 (Zhang *et al.* 2008). The ROSE algorithm was used to define super-enhancers (SEs) (Whyte *et al.* 2013), and a stitching size of 12.5 kb was applied for calculations. The identification of neighboring enhancer elements were reproduced by overlapping H3K27ac and ChIP-seq peaks and ranked by H3K27ac signals to identify an inflection point. Enhancers above and below the inflection point were defined as super-enhancer and regular-enhancer (REs) peaks, respectively, poised-enhancer peaks were genomic regions that did not overlap with H3K27ac peaks but contacted with distal promoters.

2.5. *In situ* HiC library preparation and data preprocessing

The employed in situ HiC method was described previously (Rao *et al.* 2014). The fresh muscle tissue was homogenized with liquid nitrogen and fixed with 4% formaldehyde for 30 min at RT. Fixation was quenched with the addition of glycine to a final concentration of 0.2 mol L^{-1}. After 5 min the cells were washed three times for 5 min in cold 1×PBS. Next, lysis buffer (10 mmol L^{-1} Tris-HCl pH=8.0, 10 mmol L^{-1} NaCl, and 0.2% Igepal CA630 with protease inhibitors) was added to crosslink cells, which were then incubated on ice for 15 min until nuclei were released. This mixture was then centrifuged at 1,500 r min^{-1} for 10 min at 4°C, and pelleted nuclei were resuspended in 1×NEBuffer 2 with 0.1% SDS and incubated at 62°C for 10 min. This mixture was quenched with 10% Triton X-100 (1% working concentration) for 15 min at 37°C to quench the SDS, and the obtained chromatin was digested with MboI overnight at 37°C. The blunt end DNA fragments were marked with biotin and proximity ligated, followed by a de-crosslink step with Proteinase K at 65°C overnight. The DNA washed with nuclease-free water was then sheared to 300–500 bp using a Bioruptor sonicator (Diagenode, Belgium), and purified and sized-fractioned with AMPure XP beads. Biotinylated DNA fragments were pulled down with streptavidin beads and prepared for Illumina library construction, which was performed with an NEBNext DNA Library Prep Kit (Illumina, San Diego, CA). A final amplification was performed with Herculase II Fusion DNA Polymerase, and was followed by purification with Agencourt AMPure XP beads. The resulting in situ Hi-C library was quantified and sequenced on an Illumina HiSeq X Ten platform (Novogene, Beijing) with a 150 bp paired-end length.

We preprocessed Hi-C sequence data using Juicer v1.5 (Durand *et al.* 2016) by alignment to Gallus_gallus 6.0 using BWA (v0.7.8) (Li and Durbin 2010) to eliminate ambiguous chimeric and non-alienable read pairs, duplicates, and otherwise low-quality alignments. Invalid pairs, such as dangling-end, relegation and self-circle were usually discarded at this step. A contact matrix was constructed at the level of genomic bins in which a continuous linear

genome was partitioned into a fixed size in intervals (i.e., 20 kb, denoted as 20 kb matrix resolution). Greater than 80% of bins (covered by 1,000 reads) were determined as optimal bin size. The resulting contact heatmap was normalized by the iterative correction and eigenvector decomposition (ICE), and the Knight-Ruiz (KR) matrix-balancing approach (Imakaev *et al.* 2012; Knight and Ruiz 2012) to remove intrinsic biases within the matrix, followed by quantile normalization using BNBC (version 1.0.0) to remove biases between samples with default parameters which described in our previous study (Jin *et al.* 2023). The reproducibility between duplicates was calculated by a weighted sum of correlation coefficients using HiCRep (Yang *et al.* 2017).

2.6. Genome-wide contact matrices construction

We divided the linear genome into a given matrix resolution (1 Mb bins and 500 kb) and counted the "observed" number of contacts between two locis (*i*,*j*) in all intrachromosomal contact matrices, defined as the number of base pairs between the center of the two loci. The "expected" number of contacts between each pair of loci were estimated by multiplying the fraction of reads containing *i* with the fraction of reads containing *j*, and by multiplying by the total number of reads. The correlation coefficient of contacts was computed by taking the observed contacts number between locus *i* and locus *j* (M_{ij}), and dividing it by this expected value for all inter-chromosomal loci excluding any intrachromosomal locus pairs. The Pearson's correlation matrix was computed from the observed/expected value for each intrachromosomal locus pair with every interchromosomal locus pair.

2.7. Chromatin 3D modeling

The 3D chromatin structure modeling by chromatin interactions derived from KR normalizing intra-chromosomal (at 100 kb resolution) and inter-chromosomal (at 1 Mb resolution) contact maps using an approximation of the multidimensional scaling (MDS) method. Default parameters of the Python package miniMDS (https://github.com/seqcode/miniMDS) were applied (Rieber and Mahony 2017). The simulation of 3D organizational structure of the genome was performed by PyMOL (version 2.5.2).

2.8. A/B compartment calling and chromosome status dynamics

Chromosome compartmentalization was determined by principal component analysis (PCA) of the normalized Hi-C contact matrix at 20 kb or 40 kb resolution (Lieberman-Aiden *et al.* 2009). In this, the positive and negative eigenvector of the first component (PC1 value) typically represented the A (active) and B (inactive) compartment in Hi-C data. The AB index, which represents the comparative likelihood of a sequence interacting with A or B, was calculated by subtracting the A and B values (Rowley *et al.* 2017). Centromeric regions were excluded in the A/B partitions since no chromatin interactions are identified by Hi-C in these regions. Sex chromosome sequences were excluded from the PCA analysis as well.

To identify switched A/B compartment regions of the genome in muscle development, we first identified regions with statistically significant variability in PC1 values using HOMER (Heinz *et al.* 2010). We then considered only regions where both biological replicates showed changes in PCA values from positive to negative or *vice versa* between adjacent time points. The obtained 16 compartment status across 4 developing time points were categorized as stable (AAAA and BBBB) and dynamic chromosome status. This allowed us to define the 20.65% of the genome that changes compartment status at least two-time points. We divided the 14 dynamic patterns into four clusters including switched on/off genes and reversibly switched on/off genes, and conducted functional enrichment analysis.

2.9. Identification of topologically associated domains (TADs)

We used a normalized contact matrix (generated by the Knight-Ruiz algorithm and quantile method) at 20 kb resolution to call domains. The Hidden Markov Model (HMM) was used to calculate the directionality index (DI) and to detect regions with biased upstream and downstream chromatin interactions (Dixon *et al.* 2012). We compared contact frequency between two loci separated by TAD borders (inter-TAD) with a genome-wide average with insulation score (IS), and distinguished the genome as topological domains, boundaries, and unorganized regions (Crane *et al.* 2015). The enrichment of protein-coding genes (PCGs) and housekeeping genes around TAD boundaries (±500 kb) were characterized. To identify stage-specific TAD boundaries, we merged the center positions of the boundaries in two samples and calculated the Spearman correlation of directionality indexes between the two stages. To compare the variation of the interaction intensity between relatively stage-invariant TADs, the contact frequency between two loci within the same TAD (intra-TAD) in consensus TADs (Malik and Patro 2019) was depicted by domain score (D-score) (Krijger *et al.* 2016), and calculated by dividing all intra TADs within the same TAD by the sum of intra and inter TADs on certain chromosomes. TADs were defined as having over 70% TAD bins belonging to the A compartment).

2.10. Identification of putative promoter-enhancer interactions and estimation of mediated gene expression regulation

Hi-C interaction frequencies were used to construct a normalized contact matrix (using Knight-Ruiz algorithm and quantile method) using Juicer v1.5 (Durand *et al.* 2016) and to define promoter-enhancer interactions (PEIs) using PSYCHIC v1.0 (Rosa-Garrido *et al.* 2017) at 5 kb resolution. Specifically, the normalized contact matrix was split into a smaller matrix that consisted by 20 Mb×20 Mb bins and 10 Mb steps of overlapping length, the putative enhancer regions were bins that significantly interacted with the promoter region that ranged from 2,000 bp upstream to 500 bp downstream of the TSS. Interaction pairs with high confidence (FDR values<0.01 and interaction distances≥15 kb) was defined as putative PEIs. The regulatory potential score (RPS) was defined to weigh the regulation potential of enhancers

to protein-coding genes, and the weighted sum of spatial interaction strength of multiple enhancers and a single promoter was used to estimate the gene expression (Chen *et al.* 2022). The value of RPS=Σn[$\log_{10}$(Enhancer power)], n represented the number of enhancer, the enhancer power calculated by the number of observed contacts minus the number of expected contacts. And RPS with the cutoff $|\log_2 FC|>1.5$ and $|\Delta RPS|>3$ were identified as differential RPS between 2 developmental stages.

3. Results

3.1. Skeletal muscle during development

To explore the phenotype changes of skeletal muscle during development, we prepared muscle tissue sections at the 12 developmental stages listed above. Fetal myoblasts and developed primary fibers increased at E9, and secondary fibers and myotubes were observed at E15 and E18, respectively. Also, multinucleated muscle fibers formed at E20, and the number of myofibers is determined at this stage (Fig. 1-B).

The histological appearance of muscle changed dynamically with the developmental process (Fig. 1-C and D), which is consistent with the general growth patterns of poultry (Knížetová *et al.* 1995). The morphological dynamics in our study paralleled myogenesis, occurring with the appearance of two waves as the number of muscle cells increases through hyperplasia (Fig. 1-E), which refers to myoblasts are proliferating, differentiating into multinucleated myotubes and forming muscle fibers, followed by muscle mass increase *via* hypertrophy during adult myogenesis (Bryson-Richardson and Currie 2008).

3.2. Dynamic mRNA expression changes across skeletal muscle development

RNA-seq was used to further characterize the dynamic changes of the transcriptome during skeletal muscle development. A total of 32 libraries generated 2,900 million high-quality reads with an average depth of 13.60 Gb per library (Appendix A). Together with the reference protein coding gene (PCG) set of the GRCg6a assembly (16,779 in total), ~11,819 (70.44%) of them showed evidence of transcription (TPM>0.5 in at least two biological replicates). Particularly abundant expression of PCGs was detected in embryogenesis (descended from 79.59% at E9 to 64.75% at Y8) (Appendix B-a). Hinting cells became more differentiated over time, and the heterogeneity of pectoral muscle cells decreased gradually as development proceeded.

The hierarchical clustering and t-distributed stochastic neighbor-embedding (t-SNE) analysis of the expressed PCGs revealed a similar developmental-stage dependence (Fig. 2-A and B). The early embryogenesis phases (E9, E12, and E15) exhibited secondary generations of myogenic cells, and the late embryogenesis phases (E18, E20, and D1) exhibited the fetal myoblast adult pattern. The adolescence phases (D36 and D100) exhibited a sustained conspicuous gain of weight, followed by a slow decrease for a longer period in adult phases (D300, Y3, Y5, and Y8) (Fig. 2-B; Appendix B-c and d) (Knížetová *et al.* 1995). This progression was consistent with the morphological dynamics and delineated the chronological pattern more intensively.

We performed pairwise differential expression analysis for the 12 developmental stages. We found that fewer DEGs (from 30 (for comparison between E20 and D1) to 628 (for E9 and E15)) were detected among early embryonic stages (E9, E12, E15), late embryonic stages (E18, E20, D1), adolescence stages (D36, D100), and middle-aged and aged stages (D300, Y3, Y5, Y8). Also, samples from early embryonic stages had the most divergent expression from middle-aged and aged stages (Appendix B-e). In addition, only 58 genes (~34.52%) (Appendix B-f) of the most abundant genes (168 genes in the top 1%) for a given stage were shared throughout the 12 stages. These genes were commonly enriched in the *cytosolic ribosome*, *contractile fiber*, and *ATP metabolic* processes, and were also relatively highly involved in the muscle system process for embryonic stages (Appendix C-a). These results reflect the differences in biological functions occurring in skeletal muscles during stepwise development.

We next investigated possible developmental scenarios for gene expression throughout skeletal muscle development. Here we identified nine predominant patterns associated with 2,366 genes using the maSigPro-GLM algorithm (Nueda *et al.* 2014) by *K*-means analysis (R^2>0.6, P<0.001) (Fig. 2-C), which were defined as DDGs (development dynamic genes). We found a total of 1,751 genes (219, 339, 683, 342, and 168 genes in clusters 1, 4, 5, 7, and 9 respectively) exhibited a decreased level of expression during skeletal muscle development. Most significantly were genes in clusters 1 and 7 that were up-regulated in the E9 stage. Functional enrichment analysis using the Metascape tool suggested that these genes are mainly involved in processes of *skeletal development* (such as skeletal system morphogenesis, actin cytoskeleton organization, cartilage development; skeletal system development, osteoblast differentiation, cartilage morphogenesis, tissue morphogenesis, appendage morphogenesis). A set of muscle-related genes ((*MYO6* (neuromuscular junction factor), *BMP2/5* (myokines), *PRRX1/2* and *HOXA3/10/11* (homeobox)) were incorporated, this likely reflects myogenic cell appearance, proliferation, and differentiation in early embryonic stages (Fig. 2-D; Appendix C-b). Also, a total of 381 genes (214 and 267 genes in clusters 2 and 3, respectively) were generally up-regulated in the early embryonic stages ((*AGRN* (neuromuscular junction factor), *HOXC8/10* (homeobox), *COL5A1/2*, *COL1A2*, and *ANXA2/5* (myokines)), probably reflecting the rapidly increasing number of myoblasts in the early embryonic stages (Fig. 2-D; Appendix C-c). In addition, a total of 134 genes (48 and 86 genes in clusters 6 and 8, respectively) were generally up-regulated during skeletal muscle development. Of these, specific genes in two clusters exhibited the highest expression level in the Y8 stage than other stages (Fig. 2-C; Appendix C-d). Genes in cluster 6 were mainly involved in processes of the PID IL12 2PATHWAY which include *NLRC3*, *TNFRSF25*, *IKZF3*, *IL2RB* etc. Genes in cluster 8 were mainly involved with muscle-related metabolic processes (Jejurikar *et al.* 2006; Dethlefsen *et al.* 2018), especially some myokines (such as *PGM1*, *AK1*,

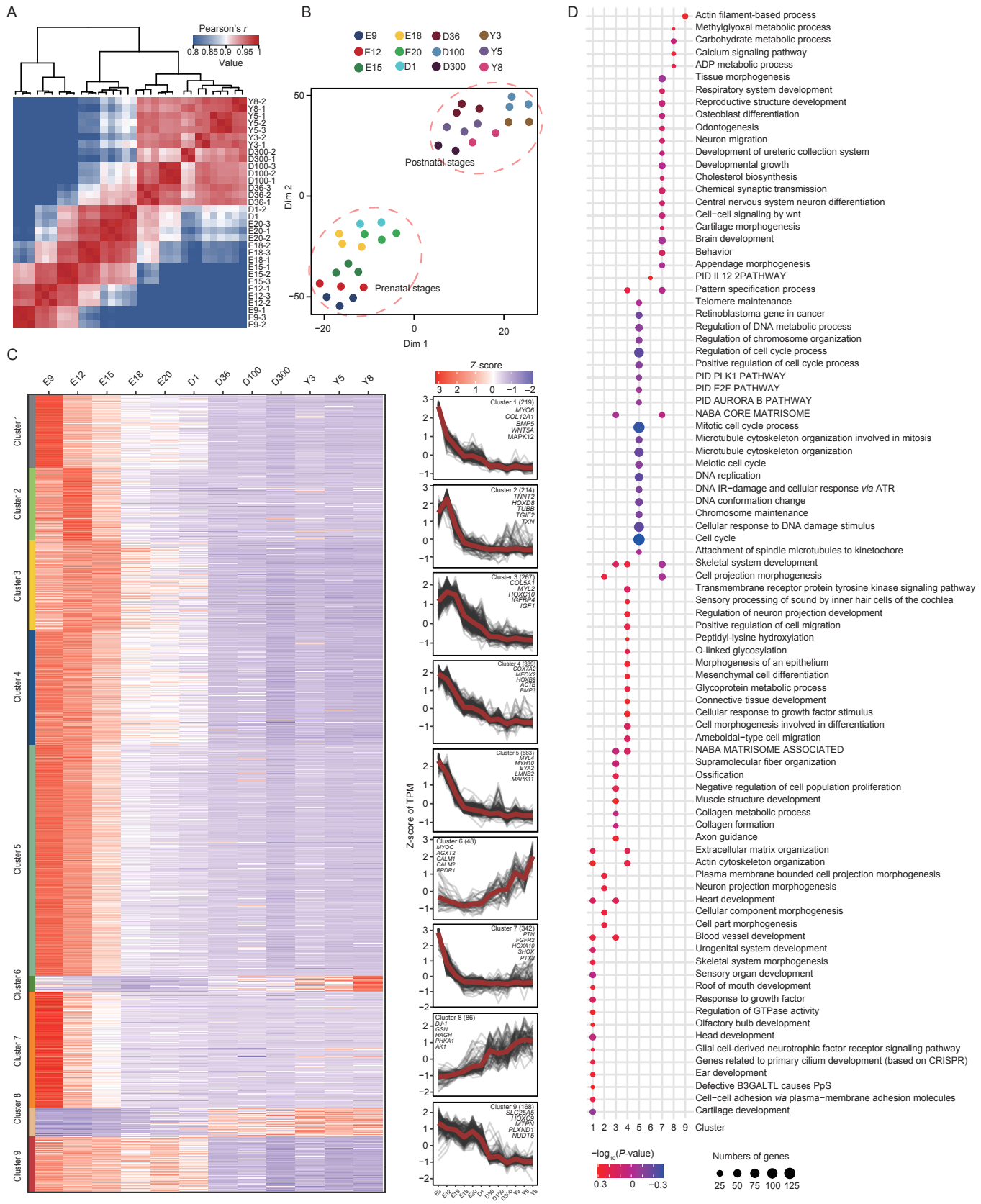


Fig. 2 Dynamic gene expression during skeletal muscle development. A, hierarchical clustering analysis of gene expression in 12 stages. B, t-distributed stochastic neighbor embedding (t-SNE) analysis of gene expression across 12 stages. C, heatmap of significant developmentally dynamic genes (DDGs) which were classified into nine clusters (left panel) with trends of gene expression along each stage (right panel). The red line represents mean gene expression levels of all DDGs for each cluster, and the black lines represent gene expression levels for each gene in the relative cluster. The number of DDGs and representative genes related to skeletal muscle is marked at the top right corner of the trend chart for each cluster. D, functional enrichment of genes for each cluster.

GSN ATP2A3, and *GLO1*) and mitochondrial located genes (*MYOC*, *TMEM223*), specifically expressed in the skeletal muscle genes *MYBPC2* and *MYOZ3*. Examples include the *calcium signaling* pathway, the *methylglyoxal metabolic* process, the *ADP metabolic* process (Fig. 2-D), hinting genes upregulated in aging chickens probably participate in the immune response of T cell and lymphocyte (cluster 6) and skeletal muscle metabolism (cluster 8). These findings reveal a dynamic gene expression pattern in a developmental stage-dependent manner, relating to functional divergences during skeletal muscle development and senescence (from embryonic period, to youth, and to old age).

3.3. Initial characteristics of chromosomal conformation in chicken genomes

To determine the dynamic changes of 3D chromatin organization mediated by gene expression during skeletal muscle development, we performed in situ Hi-C and ChIP-seq (H3K27ac and H3K4me3) assays for muscles from four representative stages, including the early (E12) and late (E18) stages of the embryo, a juvenile stage (D36), and an aging stage (Y8) (Appendix D). These four stages represent well-characterized transitions in morphological and gene expression that corresponded to primary and secondary myofiber formation, the critical period of the muscle development and aging phases.

As a result, a total of ~2.72 billion significantly aligned contacts (with a depth of 340.34 million contacts per library) were generated by eight *in situ* Hi-C libraries. Of these, ~68.87% (~1.88 billion) were intra-chromosomal contacts that were dominated by ~68.70% long contacts greater than 20 kb (Appendix E-a–d and Appendix F). Normalized intra-chromosomal contact maps at 20 kb resolution (~96.63% of bins had 1,000 or more reads) were both generated and confirmed by the high reproducibility within biological replicates (HiCRep r>0.93), and were consistent with the hierarchically clustered results deduced from the RNA-seq results (Appendix G and Appendix E-e–h).

We then constructed genome-wide chromosomal contact maps by dividing the genome into 500 kb regions, revealing that the chicken chromosomes have a similar likelihood to mutually contact each other during development. We divided all autosomes into 3 types including large (Chr.1–5), medium (Chr.6–13), and small (Chr.14–33) to delineate their features. The same type of chromosomes tended to be self-associated, small gene-rich chromosomes preferentially contacted each other more frequently, and more intensive interaction were observed within the same type of chromosomes than that of inter types of chromosomes (Fig. 3-A and B). And widespread genomic contacts were generally associated with chromosomal ends (Appendix E-i and j), which revealed the existence of chromosome territories (Gupta *et al.* 2015; Li *et al.* 2022a, b). The 3D structures initially revealed the radial locations of chromosomes within the nuclear space, further supporting the territorial architectures in chicken genome. Interestingly, visual examination showed that GC-rich chromosomes, which are usually transcript-rich (e.g., chromosome 17 has a 45.82% GC content and harbors ~27.59 PCGs per Mb), were preferentially found in the interior of the nucleus, while typically transcript-sparse, GC-poor chromosomes (e.g., chromosome 1 with a 40.29% GC content harbors ~11.36 PCGs per Mb) preferentially localized in the nuclear periphery (Fig. 3-C).

3.4. Developmental changes in compartmentalization and local accessibility for skeletal muscles during development

At the compartment level, Pearson's correlation between two intrachromosomal contact maps confirmed previous studies (Li *et al.* 2019; Li *et al.* 2022a, b) — each chromosome can be divided into two types of regions. One type, here referred to as compartment A [which constitutes approximate 50.53–57.69% (0.53~0.601 Gb) of the chicken genome] is substantially enriched for the presence and expression of genes, as well as for a high GC content (Appendix H-a–c; Fig. 4-A). Displaying the opposite properties is compartment B, which is less accessible and constitutes 42.31–49.47% (0.44–0.52 Gb) of the genome (Fig. 4-B). More compartment A were defined for small chromosomes (Appendix H-d), which were characterized by GC- and transcript-rich genomes with lower expressed genes. These known features provide an opportunity to explore the dynamic change in patterns of compartmentalization during skeletal muscles development. Hi-C libraries (with 2 biological replicates for each stage) were merged to obtain high-resolution mapping of changes in spatial chromosomal configuration and corresponding gene expression dynamics. The resulting Hi-C contact maps within replicates showed high reproducibility (Pearson correlation coefficient R>0.963 within replicates at 500 kb resolution) (Fig. 4-C).

We identified 792.18 Mb simultaneous stable genomic regions in the four periods, which were categorized as stable (AAAA and BBBB) chromosome status. And observed dramatic spatial plasticity in the arrangement of A/B compartments during skeletal muscle development (including 3,099 genes) (Fig. 4-D and E). This was accompanied by significant increasing changes in transcriptional levels of genes located in B to A than that of A to B compartment-switched regions between adjacent stages (Fig. 4-F). A total of 258.30 Mb (24.59% of the genome) was dynamic across four stages, among which A/B transitions of 146.98, 109.54, and 78.08 Mb were detected in the comparisons of E12 *vs*. E18, E18 *vs*. D36, and D36 *vs*. Y8, respectively (Fig. 4-E). Among the 3,163 DEGs, there were 602 DEGs located in 12.04 Mb of genomic regions (~1.15% of the chicken genome) underwent compartments switch (Appendix H-e and f). Dynamic compartmentalization during muscle development were observed, and relative changes in gene expression were likewise seen. The most significant differences in gene expression undergoing compartmental switching are shown in Fig. 4-F. Although the proportions of compartment A and B in each stage were stable (Fig. 4-B), a gradual loss of local interactions in heterochromatic regions was observed during senescence, and the compartment states were more discontinuous in the Y8 senescence stage compared with these embryonic stages.

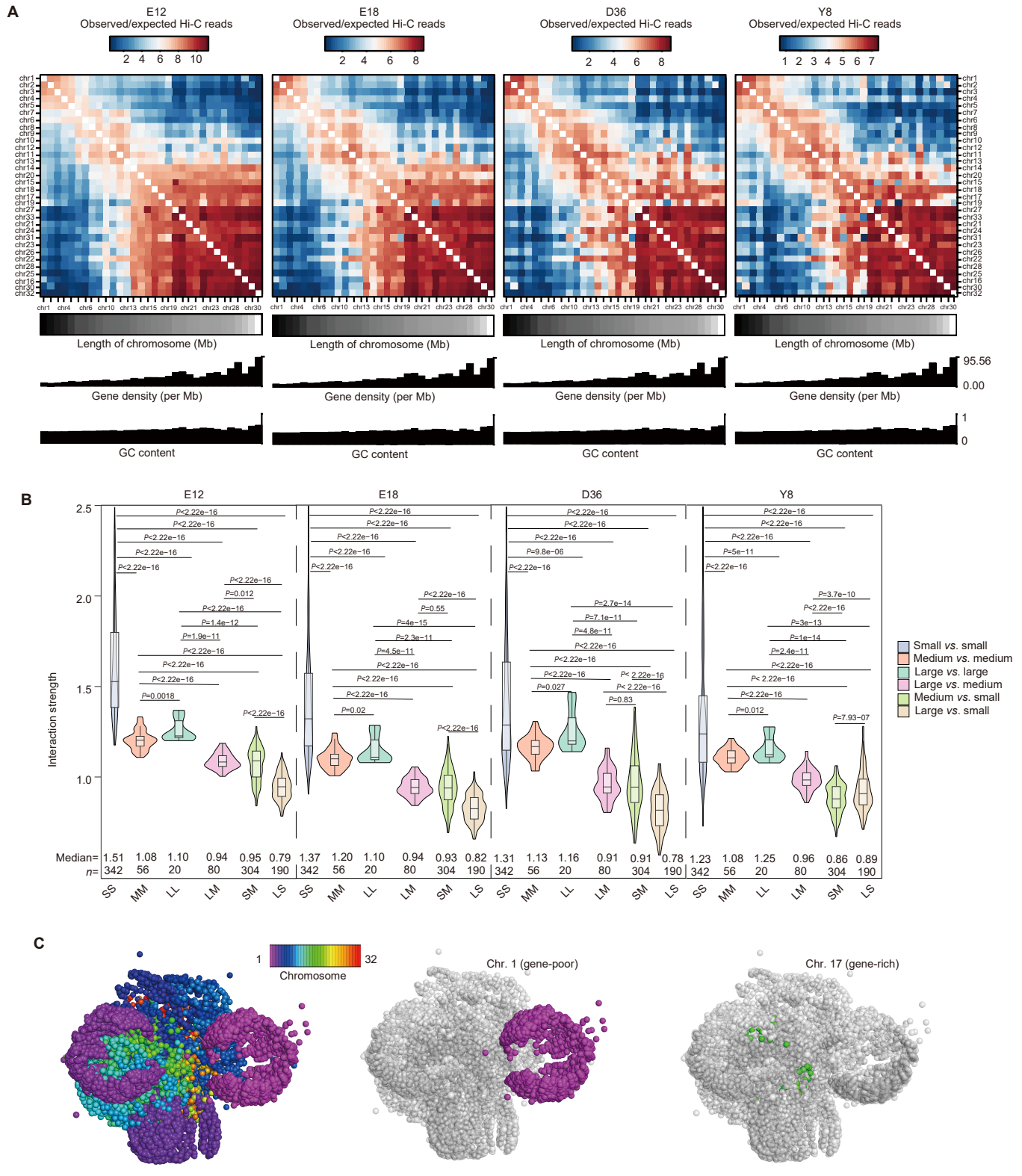


Fig. 3 Overview of 3D organization in chicken skeletal muscle during development . A, observed/expected contact matrices between chromosome pairs. Also shown are the length, gene density, and GC content of each chromosome. B, normalized contact intensity within and between large (L), medium (M), and small (S) chromosomes. *P*-values were calculated using the *t*-test. C, examples of 3D chromosome conformations in the nucleus of chicken skeletal muscle of representative stage E18.

In addition, the 3,099 genes involved with the dynamic chromatin state were designated as six patterns to investigate their temporal changes (Appendix I). Genes in cluster 1 (621) and cluster 3 (690) exhibited a transcriptional activation pattern (B to A), where the B compartment in the early embryonic stage gradually switched to the A compartment

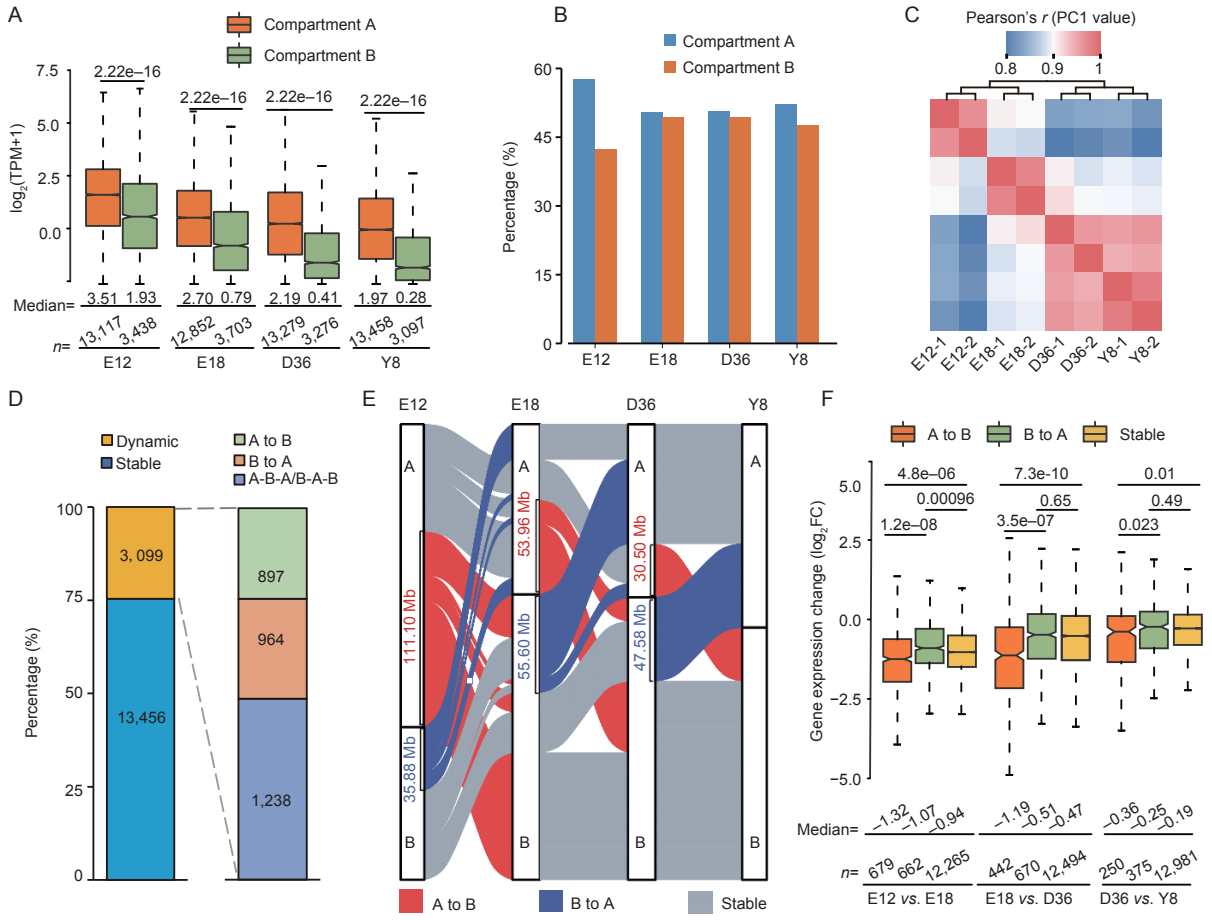


Fig. 4 Compartmentalization dynamics in chicken skeletal muscle during development. A, expression levels of genes located in A/B compartments. B, A/B compartment percentages of each stage. C, heatmap of the correlation coefficient between Hi-C contact maps of consecutive stages evaluated by PC1 values. D, proportions of stable and dynamic compartments, and the number of genes in these regions. Dynamic compartments are classified into three types of transitions. E, genomic lengths and dynamic compartments changes during development . F, expression levels of genes located in compartment switching regions (from A to B (orange), from B to A (green) compared to those in stable compartments (yellow). TPM, transcripts per million. FC, fold change. *P*-values were calculated using the *t*-test. In the boxplot, the internal line indicates the median, the box limits indicate the upper and lower quartiles, and the whiskers extend to 1.5 IQR from the quartiles.

status thereafter (Appendix J). We observed a set of genes associated with the inflammatory response and disease in cluster 1, such as *IL7*, *STAT1*, *NFKB2*, *CD86*, *KIT* (Fig. 5-A), *CHUK*, *MMP1*, *PIK3CB*, *PLCG2*, *CXCL8*, *ITGA2*, and *MECOM*. Specifically, the protein encoded by *CTNNA3* plays a role in cell-cell adhesion in muscle cells, and *CTNNA3*-mutations are associated with cardiomyopathy (Janssens *et al.* 2003; van Hengel *et al.* 2013). The variants of S*ORBS2* (Fig. 5-B) are responsible for cardiomyopathy (Li *et al.* 2020; Liang *et al.* 2021) and is capable of inducing premature senescence in primary human fibroblasts (Liesenfeld *et al.* 2013). Genes in cluster 3 were mainly involved in the processes of the regulation of early development and growth (such as embryonic morphogenesis and cell division). For example, (1) proteins encoded by *MYOM2*, *MYPN*, and *MYH10* are the major structural components of sarcomeres. (2) *LBX1*, *MYF5*, and *MYF6* are involved in muscle differentiation. (3) *HOXD12* and *HOXD13* play an important role in morphogenesis. (4) *IGFBP1*, *TGFA*, *TGFB1*, and *TGFBR3* are responsible for growth.

In contrast, genes in cluster 4 (510) and cluster 6 (472) were down-regulated (change from compartment A state to B) across development. They were particularly enriched in processes of skeletal muscle development, including cartilage development, skeletal system development, muscle organ development, and actin cytoskeletal organization). Typically, *EYA1* and *EYA2* (Fig. 5-C) are required and down-regulated during myogenesis in chicken (Grifone *et al.* 2007; Ishihara *et al.* 2008; Doi *et al.* 2012). *BMP3*, *BMP7*, and *BMP10* are essential for bone development. In addition, *SOX6* (Fig. 5-D) is a transcription factor that plays a pivotal role in fiber type specification, suppressing transcription of slow-fiber-specific genes during fetal myogenesis (Quiat *et al.* 2011; Taglietti *et al.* 2016).

Similarly, genes with an intermediate transition (cluster 2 with 328 genes, B to A to B) were enriched in skeletal system development, muscle tissue development, bone development, and actin cytoskeletal organization, reflecting a functional transition across muscle development and aging. *WNT* has been implicated in several developmental

processes, and the sequential activation *HOX* was essential for limb development (Noordermeer *et al.* 2014). Genes with another intermediate pattern (cluster 5 with 478 genes, A to B to A) are associated with the processes of neural activity (such as chemical synaptic transmission and synaptic vesicle localization). *MYO5C* and *MYO5A* are abundant in nerve cells.

3.5. TAD alterations are tightly coupled with transcriptional changes

TAD is a distinct 3D chromatin domain with functional relevance to transcriptional regulation. Genomic loci within TADs encounter each other more frequently than with loci outside (Dixon *et al.* 2012). We used the chromosome-wide insulation score (IS) and the directional index (DI) to identify TAD boundaries, which were highly reproducible within biological replicates (Pearson's *r* (IS)>0.93 and Pearson's *r* (DI)>0.88) (Appendix K-a and b). In result, we detected 1,758–1,908 TAD boundaries across chicken muscle development, and ~98.03% TAD boundaries were invariant during skeletal muscle development (Fig. 6-A), indicating that TAD is a conserved chromatin structure, which is consistent with previous reports (Yuan *et al.* 2021; Chen *et al.* 2022). Von Neumann Entropy (VNE), which measures changes of structural order of intra-chromosomal contact (Lindsly *et al.* 2021), was gradually decreased with development (Fig. 6-B). This indicates a more structurally permissive (disorder) of genomes, which might result from the higher pluripotency of less-defined cells in the chromatin during the early embryonic development stages.

A total of 89–92% of the genome was partitioned as TADs, and we characterized intra-TAD interaction kinetics by applying a domain score (*D*-score) as was reflected by the tendency for interactions within a given TAD. The difference of interactions within TADs also showed a good biological replication within stages (Pearson's *r* (*D*-score)>0.94,

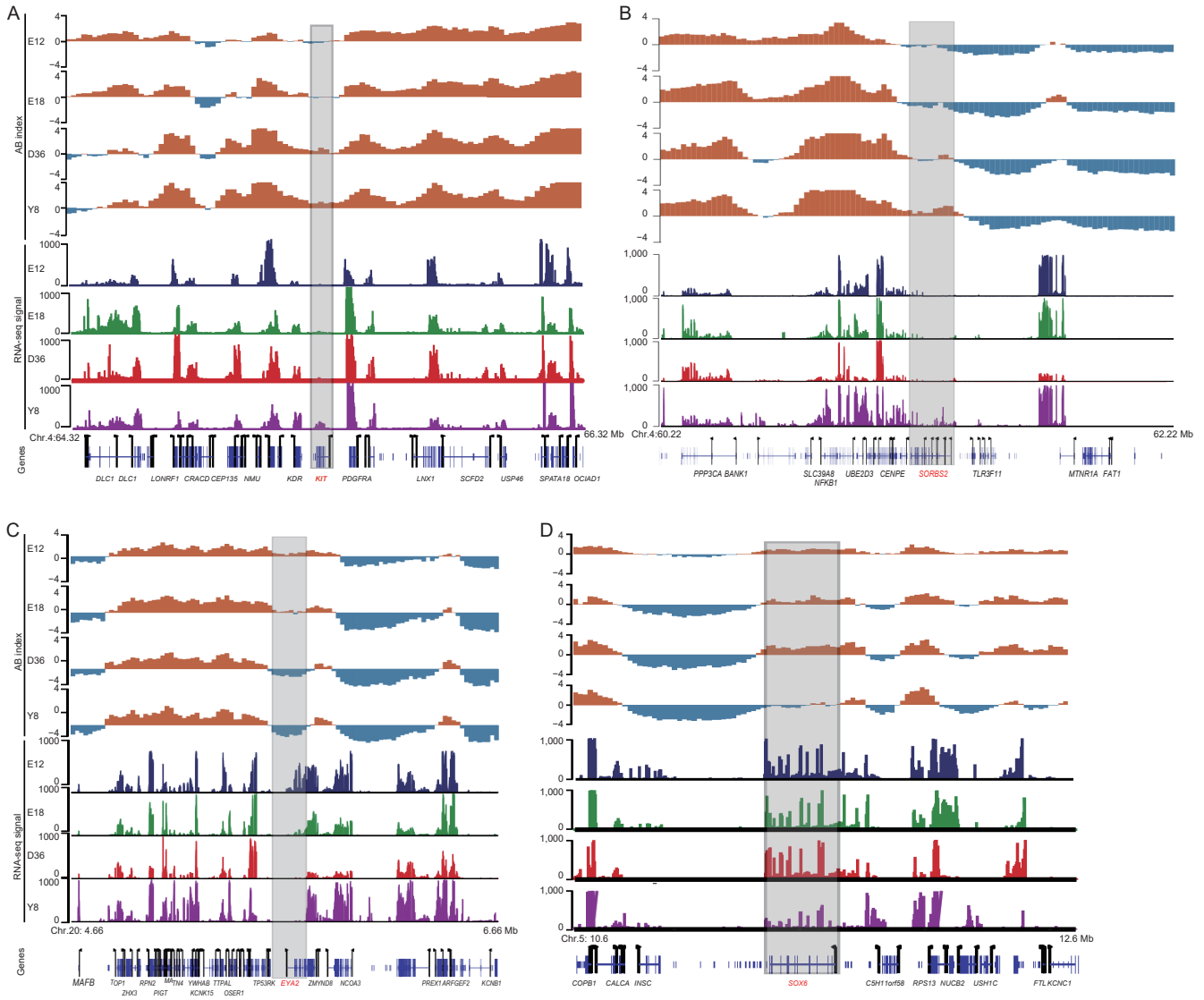


Fig. 5 Four representative functional genes undergo compartment switching during skeletal muscle development, including gene *SORBS2* (A), *KIT* (B), *EYA2* (C), and *SOX6* (D). The shaded boxes indicate the chromosomal locations of the genes. The tracks show the compartment status (top), and and RNA-seq signal (bottom) of the genes. Gene structures are indicated below the tracks.

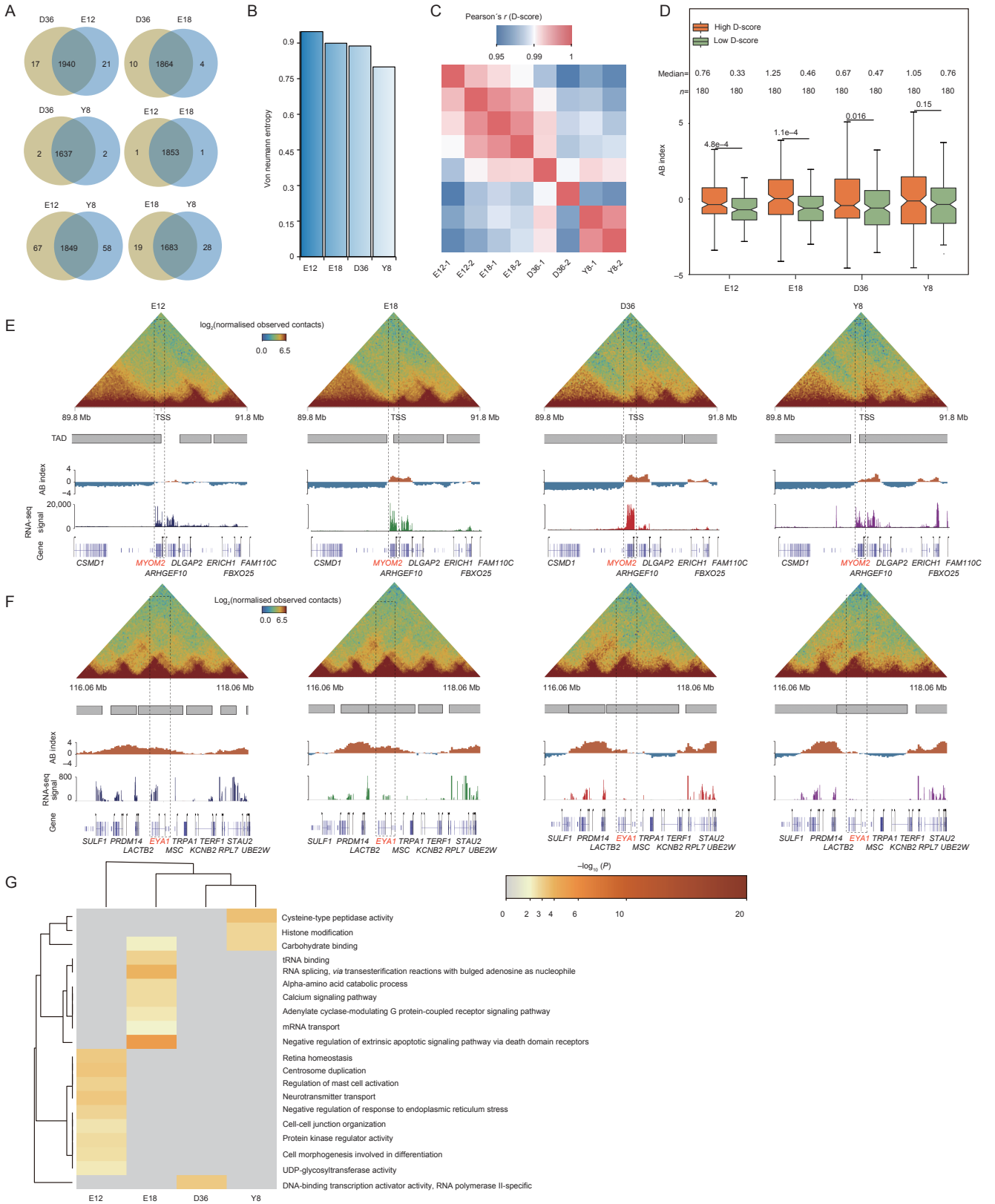


Fig. 6 Characteristics and function of topologically associated domains (TADS) in chicken skeletal muscles. A, overlap of TAD boundaries between different stages. B, heatmap of correlation coefficient between Hi-C contact maps of consecutive stages evaluated by *D*-score values. C, quantification of disorder in the chromatin structure of the whole genome using Von Neumann Entropy (VNE). D, AB index of bins with a relatively low and high *D*-scores of consensus TADs. *P*-values were calculated using the *t*-test. E–G, dynamic TAD interaction changes accompanied with gene expression changes across different developmental stages. *MYOM2* (E), and *EYA1* (F) in the relative TADs are shown. Top: Hi-C contact heatmaps of the genomic region around *MYOM2* (E), and *EYA1* (F). Bottom: Genome browser tracks of TAD locations, AB index, and RNA-seq signals. G, functional enrichment of genes in stage-specific boundaries for each stage.

Pearson's *r* (IS)>0.93 and (DI)>0.88) (Fig. 6-C; Appendix K-a and b). We next called 1,809 consensus TADs with an average size of 520 kb in chicken muscle. TADs (~2,000) with an average size of 460 kb in E12 (2,094), E18 (2,124), D36 (1,995), and Y8 (1,973) were called by DI and IS algorithms. Consistent with previous findings, the number of TADs observed in our data decreased during development, along with a corresponding increase in size although the numbers and sizes of TADs were similar across development (Appendix K-c). Also, the number of compartment A TADs was greater than that of compartment B. In addition, compartment A TADs were ~0.82 times smaller (P<0.0001) than compartment B TADs (Appendix K-d) for all stages, indicating that local chromatin architecture correlates to more active gene regulation by local interactions in these gene-dense regions (Li *et al.* 2022a, b).

We also found that chromatin distributed by the consensus TADs with relatively higher *D*-scores were preferentially accessible (with higher AB index) (Fig. 6-D). The expression of genes and size of TADs distributed on large chromosomes were higher than that of small ones although their *D*-score increased with the large, medium, and small chromosomes (Appendix K-e–g). Furthermore, to investigate dynamic patterns of TADs that substantially reflect the intra-TAD compartmentalization and transcription changes, we identified 31.02% (662 TADs, 316.57Mb) that display significant alterations of development across successive periods (Appendix L-a). Among which, we further defined 149 DEGs that spanned 71.88 Mb (~6.84%) of the genome characterized by altered TADs (Appendix H-e and f). All dynamic TADs were contrasted as two representative connectivity patterns, with *D*-scores either up or down. For example, clusters 1, 2, and 6 (322 TADs) exhibited ascendant connectivity accompanied by most genes undergoing B to A compartment switching, while descendant connectivity was seen in 339 TADs in clusters 3–5 (with major genes switching from A to B compartments) (Appendix L-b and c). In addition, we found the average expression of all genes in dynamic TADs were decreased during chicken muscle development. Which was consistent with the expression patterns illustrated in Fig. 2-C that overwhelming majority genes were down-regulated, and very few genes were up-regulated. Genes undergoing B to A transition (such as *KIT*, *NMU*, *MYL9*, *INPP5F*, *P2RX6*, *P2RX2*, *SMTN*, *SORBS2*) were associated with muscular movement (such as smooth muscle contraction, microtubule-based movement, and ion channel activity) (Appendix L-d and e), while gene transcription with A to B switching (*CACNA1H*, *SKI*, *EYA2*, *RBM38*, *NFATC2*, and *SOX6)* was involved in development (Appendix L-f and g). This demonstrates that chicken muscle development was accompanied by intra-TAD changes with switched compartments.

We further focused on these genes that showed a TAD boundary change. For example, *MYOM2* is a major component of the myofibrillar M-band of sarcomere, and a hub gene within interactions of sarcomere genes. The myomesin appeared from E7 and continuously accumulated throughout chicken pectoral muscle development (Grove *et al.* 1985), it might interfere in muscle integrity and cardiomyopathy (Lamber *et al.* 2022). The interaction frequencies enhanced and formed TADs boundary rearranged, along with the enhanced gene expression of myomesin-2 during development (E12 to D36) (Fig. 6-E). Furthermore, *EYA1* is required and down-regulated during myogenesis in chicken (Grifone *et al.* 2007; Ishihara *et al.* 2008; Doi *et al.* 2012), which functioned in constrained smaller TADs in embryonic stages (Fig. 6-F). *SNTA1* associates with dystrophin at the neuromuscular junction and alters intracellular calcium ion levels in muscle tissues. Also, *DNAJB6*-mutated animals are more likely to develop myopathies. Histone modification and cysteine-type peptidase activity were enriched in E18-specific genes, and *NEXN* localizes to Z-discs and is expressed in striated muscle (Zhu *et al.* 2018). RNA polymerase II-specific DNA-binding transcription activators were enriched in D36, and an apoptotic signaling pathway was found in Y8-specific biological processes. Particularly, disorders of fibrinogen genes (*FGB*, *FGA*, and *FGG*, located in the Y8-specific boundary) can result in quantitative afibrinogenemia, hypofibrinogenemia, or functional dysfibrinogenemia diseases (Tiscia and Margaglione 2018). Our pair-wise functional analysis for these genes identified a sub-set with stage-specific comparisons of TAD boundaries, showing that cell differentiation and neurotransmitter transport are E12-specific categories (Fig. 6-G).

3.6. Dynamic PEIs of transcription-linked genes

The regulatory specificity of enhancers and their interaction with gene promoters is thought to be controlled by their sequence and the binding of transcription factors (Kragesteen *et al.* 2018). To investigate the regulatory potential of enhancers to muscle-related PCGs, we identified a set of putative promoter-enhancer interactions (PEIs) (from 27,020 of Y8 to 29,183 of E18) which were assigned to substantially expressed PCGs (7,562 of E18 to 8,139 of Y8) (Appendix M-a) at 5-kb resolution (Appendix M-b). Approximate 60% of these were short-range contacts within 100 kb (Appendix M-c). We observed that ~65.48% of putative enhancers skipped the neighboring promoter and interacted with distal target gene promoters, and ~74.42% of PEIs were constrained within TADs (Appendix M-d).

We next characterized certain enhancers as either poised enhancers (PE, those depleted of H3K27ac peaks), or super-enhancers (SE) which formed larger domains with higher H3K27ac levels, as compared with regular enhancers (RE). Genes mediated by active enhancers (SEs and REs) decreased with development (E12: 78.69%, E18: 65.95%, D36: 46.51%, and Y8: 41.95%) (Appendix M-e). Among the average of 27,643 putative PEIs, we detected 51.37% (14,370) H3K27ac-enriched signals across the 4 developmental stages. Genes interacting with multiple enhancers exhibited higher expression, which hinted the effect of enhancers on actively transcribed target genes during development (Appendix M-f).

We further applied a regulatory potential score (RPS) of genes in order to explore the regulatory effects of multiple enhancers on certain genes, and to depict the dynamic rearrangements of chromatin folding accurately (Li *et al.* 2022a, b). The RPS exhibited similar stage-

dependent patterns with gene transcription, as well as compartmentalization and TAD connectivity. A higher RPS was accompanied by higher transcription activities (Appendix M-g), higher RPS and gene transcription were observed on large chromosomes compared with small chromosomes (Appendix M-h and i). Suggesting the expression of genes mediated by an enhancer largely contributed by the total effect of all enhancers.

In addition, 59.35% (16,384) of the promoters were modified by H3K4me3 signal, generally, the genes regulated by SEs exhibited higher RPS (3.19–3.88) (Appendix M-j) and transcriptional levels (2.15–3.69) than that of inactive enhancers (PE) (RPS:1.83–2.04, TPM: 1.38–3.08) across development except E18 (Appendix M-k). Furthermore, compared with inactive promoters, H3K4me3 signal-enriched promoters (which were characterized by higher transcriptional activity) were more likely to interact with active enhancers (SEs and REs) excluding no enhancer signal-enriched genes at embryonic stages, and the number of interacted active enhancers decreased at postnatal stages (Appendix M-l), thus confirming the effect of enhancers on different activities of transcription. Furthermore, these active promoter-related genes exhibited a higher level of gene expression, as compared to those with inactive promoters (Appendix M-m). This indicates that the more active PEIs functioned in embryonic development (other than post-natal), hinting that stronger PEIs could be activated during myogenesis, and shut down in myofiber hypertrophy.

A total of 4,538 PCGs with significant differential gain or loss of RPS between two successive stages were identified, taking account for ~2.57% of the genome (26.97 Mb). Among which, there were 950 DEGs spanning 5.98 Mb (~0.57%) of the genome exhibited changes in PEI regions (Appendix H-e and f). The enhancer and promoter types were determined by the H3K27ac and H3K4me3 signals, respectively. These 4,538 PCGs were determined by *K*-means to cluster across development stages . Intriguingly, we obtained four canonical dynamic patterns of RPS values, and the RPS change for each cluster was characterized by a specific stage. Among them, 990 genes in cluster 1 showed an extremely high RPS enrichment, and totally interacted with enhancers at D36 stage. These were involved in the circulatory system process, muscle structure development, and developmental growth (Appendix N-a). Genes (*n*=1,097) in cluster 2 exhibited especially high RPS values at E12, and participated in biological processes such as embryonic morphogenesis, development of various organs, and muscle structure development (Appendix N-b). A set of (*n*=957) genes, whose RPS were particularly high at Y8 were included in cluster 3, and related to ncRNA metabolic processes, double-strand break repair, and chordate embryonic development (Appendix N-c). Tumor suppressor genes (*CAV2*, *SMOC2*, *KLF6*, *TSPAN32* (Williams and Lisanti 2004; Lombardo *et al.* 2019; Lu *et al.* 2019; Syafruddin *et al.* 2020), *ING3* (Chen *et al.* 2010; Molina-Privado *et al.* 2012), and *GAS8*(Pan *et al.* 2018)) were activated in aging muscle. Genes *ETS1*, *PLEKHA1*, *MEPE*, *A2M*, and *TERF2* (related to aging) (Dittmer 2003; Surakka *et al.* 2020; Ruis *et al.* 2021), *PRRX2* (which facilitates dermal regeneration and is related to muscle repair), *VRK1* (related to regulation of cell proliferation), *DDX4* (implicated in embryogenesis), and *CDH15* (which provides a trigger for terminal muscle cell differentiation) (Esteves de Lima *et al.* 2021), were upregulated during aging. The RPS of genes in cluster 4 (*n*=1,494) were very high at stage E18. The functional enriched categories were similar to genes in cluster 2, where negative regulation of cell differentiation was enriched, confirming the characters of amyotrophy in late embryogenesis (Appendix N-d). The developmental specificity that decreasing proliferative activity of satellite cells in the atrophied muscle of late-term embryos preparing for the postnatal growth (Chen *et al.* 2013), confirmed the unexpected finding that majority genes with high RPS but low transcription levels expressed at this stage (Appendix M-k). Notably, genes involved in *circulatory system process* and *muscle structure development* were enriched in D36 and E18 (cluster 1 and 4). Furthermore, to explore the contribution of PEIs to the functional properties of muscle development, we dissected the RPS, enhancer, and transcription of genes in the enriched category of *skeletal muscle development*, which was enriched in cluster 1, 2, and 4 (D36, E18 and E12). Here, enrichment decreased with development.

We found that although their expression levels were considerably high at E12, the relative RPS and active enhancer (SE and RE) were coordinately enriched at specific stages. For example, *SIX4* (regulating myogenesis in early embryonic development by mediating *PAX7* and *MyoD*) (Buckingham and Rigby 2014) (Fig. 7-A), clearly interacted with SEs at the early embryonic stage E12, and the rewiring of PEIs attenuated thereafter. The epidermal growth factor receptor (*EGFR*) is a primary coordinator of signal transduction from the extracellular environment (Kalmes *et al.* 2001; Prenzel *et al.* 2001). Previous studies confirm the involvement of surface metalloproteinases in EGFR activation during oxidative stress (Nkabyo *et al.* 2005; Stanic *et al.* 2010). Here, we found that the enhancer and promoter interacted most at the embryonic age of 18 days, so as the RNA-signal (Fig. 7-B), showing the effect of *EGFR* on myofiber proliferation and antioxidant during this period.

The vascular cell adhesion molecule-1 (VCAM-1), a mononuclear leukocyte adhesion molecule encoded by *VCAM1*, is expressed in cultured vascular endothelial and vascular smooth muscle cells in response to cytokines *in vitro* (Li *et al.* 1993). In addition, activated satellite cells (SCs) retained the expression of *VCAM1* and other genes along with the induction of proliferative and myogenic markers such as *desmin*, *Myf-5*, and *MyoD* (Sousa-Victor *et al.* 2022). Thus, we can see that *VCAM1* is regulated by enhancers after birth. At the age of day 36, muscles have a great capacity for repair with more satellite cells. During skeletal muscle senescence, the repair capacity is gradually lost (Appendix O).

LARP1B and *MEPE* were highly activated at the senescence stage (Appendix O). mTORC1 interacts with La-related protein 1 (LARP1) to specifically regulate the expression of 5′ terminal oligopyrimidine tract (5′TOP) mRNAs, which encodes proteins of the translation machinery and ribosome biogenesis. Recent studies have shown

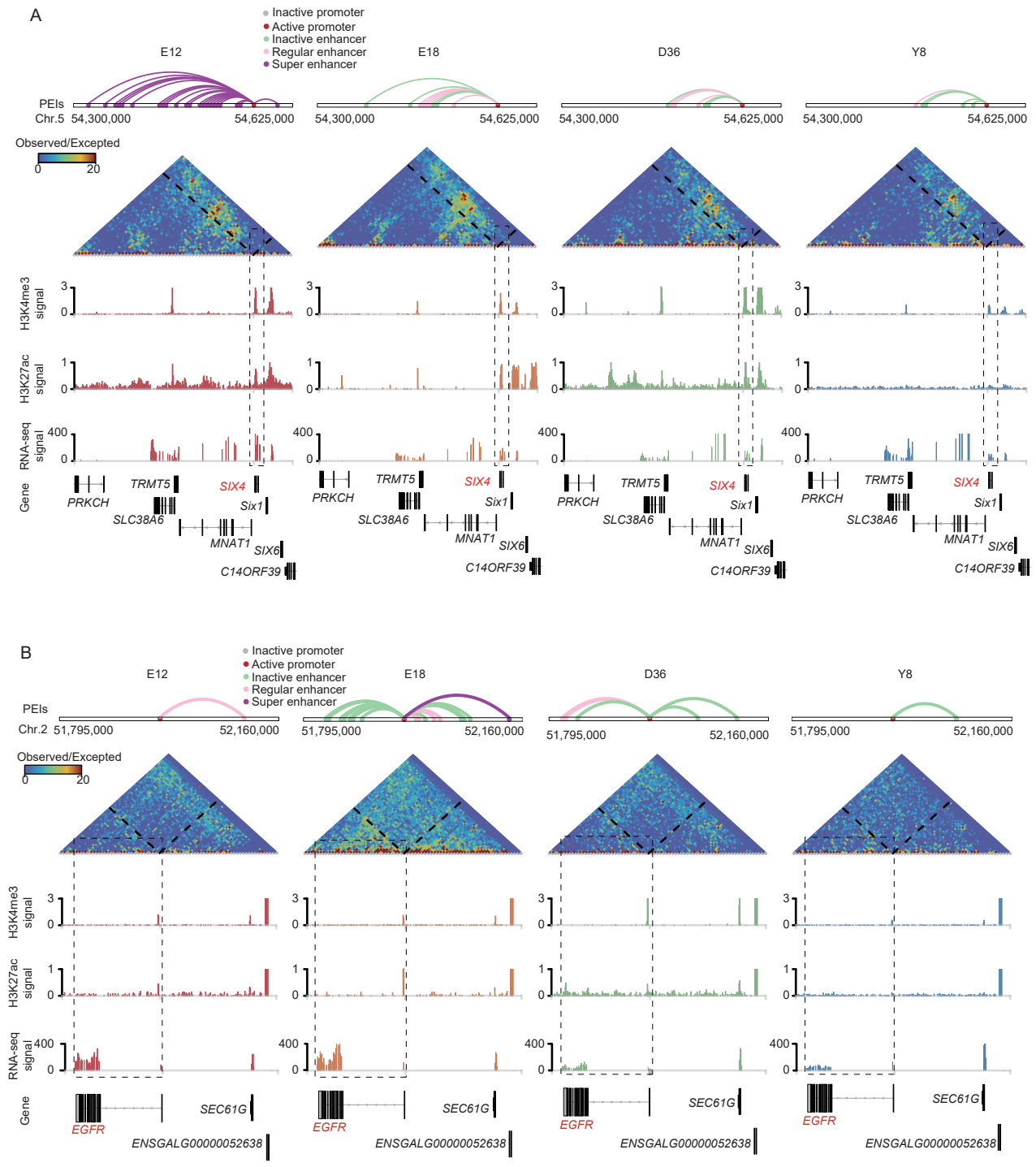


Fig. 7 Promoter-enhancer interactions (PEIs) rewired in chicken skeletal muscle during development. PEI rewiring of a functional *SIX4* (A) and *EGFR* (B) during muscle development. Top: schematics of PEIs and Hi-C contact heatmaps of the genomic region containing *SIX4* and *EGFR*. Middle: genome browser tracks of H3K4me3, H3K27ac and RNA-seq signals. Bottom: regional gene structures. The dashed line boxes indicate the chromosomal locations of the genes.

that inhibition of TOR (target of rapamycin) can extend the lifespan of adult *Caenorhabditis elegans* (Chin *et al.* 2014) and *Drosophila melanogaster* (Su *et al.* 2019). Increased matrix extracellular phosphoglycoprotein (MEPE) expression occurs in several phosphate and bone-mineral metabolic disorders (David *et al.* 2009). *MEPE* was also found associated with bone mineral density (Yau *et al.* 2021). These studies indicated the important functions of *LARP1B* and *MEPE* during skeletal muscle senescence, and that they can be useful candidate target genes for anti-aging.

4. Discussion

Hi-C technology has been widely applied into different biological fields, such as transcription regulation, cell

division, fate determination, growth, development, disease, and genome evolution. Hi-C will even be further applied to precision biology (Kong and Zhang 2019). Given the relative infancy of Hi-C data of livestock, there are no deeply sequenced Hi-C datasets available for livestock species (MacPhillamy *et al.* 2021). In order to narrow the substantial gap between model organisms and livestock in the knowledge of 3D genomic structures, and how it relates to gene regulation. We have characterized the tightly coupled alterations of genome topology with muscle-related gene expression using *in situ* Hi-C. The 3D chromatin architecture changes of chicken muscle are supported by the similar temporal patterns between phenotype and transcriptome characteristics across embryogenesis and post-natal development. Overall, the strong and distinct intensity of interactions was observed at a relatively high resolution, aligning with the occurrence of stable contact frequencies between chromosomes during muscle development. The linkages between gene activation/repression and these massive structural reorganizations are illustrated by a 24.59% (258.30 Mb) switching of A and B compartments, a 31.02% (316.57 Mb) variation of contact frequency within TADs, and a 33.15% rewiring of long-range gene interactions.

As stated in our previous study (Li *et al.* 2022a, b), shorter chromosomes are characterized by higher long-range contact probability, more stretched and less condensed chromosome territories (CTs), and stronger inter-chromosomal connectivity. Furthermore, the DNA transposons were negatively correlated with intra-TAD contact frequency in chicken, while positive correlation was found in mammals. The interchromosomal contacts were also found unequally distributed among chicken genome (Fishman *et al.* 2019).

Our findings provide an explanation for the sequential activation, repression, and intermediate transition of genes with dynamic compartmentalization. In this, most compartment A/B switching (146.98 Mb) occurred during embryonic myogenesis (E12 *vs.* E18), followed by 109.54 Mb of changes across the transition of developing muscle from fetal to post-hatch (E18 *vs.* D36), and 78.08 Mb alterations of muscle hypertrophy and dystrophy from rapid growth to aging (D36 *vs.* Y8). We found that more substantial changes of chromatin interaction occur in embryonic than in post-hatch chicken muscle. *Eya* genes, which are required for hypaxial myogenic commitment (and participate in the limb patterning of connective tissue (Xu *et al.* 1997; Grifone *et al.* 2007), were activated in embryonic periods and shut down after birth. The same is true of genes associated with early development such as *IGF-I*, *BMP*, and *WNT*. In contrast, the late activation of (1) *MYOM2* (which interconnects the major structure of sarcomeres — the M bands and Z discs), (2) *MYPN* (which interacts with nebulin in skeletal muscle), as well as (3) *MUSTN1* (which implicates myofusion, skeletal muscle growth, and repair) are accompanied by substantial changes in compartmentalization. Therefore, the fact that active chromatin dynamics are largely accompanied by changes of subnuclear compartmentalization suggests that it plays a major role in mediating the switching between the active A and the inactive B compartments.

It is well established that TADs (as finer chromatin packing structures residing in the A/B compartments) are relatively stable topological domains during development (Hug and Vaquerizas 2018; Zheng and Xie 2019), and that (because of the relative functional independence restrained by TADs delimitations) TAD-boundary regions are linked to transcriptional control (Dixon *et al.* 2012). We defined a minor portion of TAD boundaries as stage-specific (between adjacent stages) by estimating their directionality index and insulation potential, indicating that a gain and loss of topological borders might create new opportunities for gene regulation. As noted in previous study, the TADs are evolutionarily conserved gene expression regulatory units. TAD boundaries were largely invariant during porcine skeletal muscle and liver development (Yuan *et al.* 2021; Chen *et al.* 2022), so as chicken muscle development. However, we observed plasticity with respect to TADs switching between compartment A and B, irrespective of their transcriptional status according to the quantitation of D-score. Dynamic TAD connectivity changes coupled by chromatin status switching are generally consist with the biological function transition of muscle development and aging. In the human genome, genes coregulated during myogenesis are nonrandomly distributed (Neems *et al.* 2016). We found potential candidates in *DNAJB6*, *MYOM2*, *SNTA1*, *NEXN*, *LMBRD1*, and *CACNA1D*, which are muscle-related genes with stage-specific functions. Furthermore, *SKI*, *SORBS2*, *KIT*, *NMU*, and *INPP5F* are up-regulated during development, while *CACNA1H*, *P2RX6*, *P2RX2*, *SMTN*, *MYL9*, *EYA2*, *RBM38*, *NFATC2*, and *SOX6* down-regulated across chicken muscle development. This indicates a strong connection between local chromatin topology and transcription (Lieberman-Aiden *et al.* 2009).

Chromatin loops are the finest local chromatin structure that is retained within TADs. They dynamically regulate gene transcription by facilitating the approach of enhancers with their target gene promoters (Nora *et al.* 2012; Matharu and Ahituv 2015; Zhan *et al.* 2017). At the PEI level, there were ~2.57% of the genome (covering 4,538 genes) regions changed. And ~0.57% of the genome underwent changes both at PEI and transcriptional level. We also found that PEI-coupled gene expression levels were positively correlated with the number of promoters and with the regulatory potential score (RPS) of genes. Also, genes mediated by active enhancers and promoters were characterized by higher transcriptional activity. Intriguingly, three sets of muscle-related genes had an aberrant overexpression in the early embryonic period, and exhibited stronger promoter interactions with active enhancers in E12 (examples are *SIX4*, *FLNB*, *NEUROG1*, *ATP2A2*, *MYOCD*, and *GLI3*), in E18 (*EGFR*, *NEB*, *FLNC*, *EGR2*, *MYOF*, *SPARC*, and *SOX18*), and in D36 (*COL6A3*, *CHRNA1*, *VCAM1*, *SOX8*, and *TCF15*). Intriguingly, as the fact noted in previous study (Chen *et al.* 2013), muscle atrophy is a developmental specificity in skeletal muscle of late-term avian embryos. During which, the remaining yolk sac appears to be inadequate in meeting the full nutritional requirement of very mature avian embryos with their hatching activities. E18 is proximal to the time at which the chickens are about to emerge from the shell, and many genes may be activated. And we found genetic evidence contributes to the developmental characteristics

that were supported by the biological functions. Furthermore, we found numerous genes mediated by strong PEIs at Y8 to be associated with aging-related diseases (ARDs). Genetic control of muscle aging is characterized by muscle metabolism alterations (*MEPE* and *GDP1L2*) (Schrauwen *et al.* 2019; Maharjan *et al.* 2021), short telomeres (*TERF2* and *TERF2IP*) (Robin *et al.* 2020), increased physical limitations and risk for diseases (*SMARCA1*, *CASP3*, *SLC38A4*, *SCN2A*) (Huang *et al.* 2011; Sanders *et al.* 2018), and diminished regenerative capacity and satellite cell potential (*DDX4*, *BABAM2*) (Hernandez *et al.* 2015; Chung *et al.* 2020). Importantly, we found that *CAV2*, *SMOC2*, *KLF6*, *TSPAN32*, *ING3*, and *GAS8* were activated in aging muscle, which together might function to suppress tumors in response to the activation of oncogenes, and participate in the OIS (oncogene-induced senescence) (Courtois-Cox *et al.* 2008; Salama *et al.* 2014). Genes with senescence-associated secretory phenotype (SASP) with relevance to inflammation and immune response (Coppe *et al.* 2010) were found as well (examples are *NFKB1*, *NFKBIZ*, *ALCAM*, *ROBO2*, *IL1R2*, *CXCL8*, *TLR6*, *CD8A*, *CD6*, *CD40*, *OPTN*, *A2M*, *GSK3B*, and *STAT1*).

5. Conclusion

Our data indicate that dynamic changes in genome topology, including local domains and loops, may facilitate transcriptional regulation to control chicken development, implicating a conserved causality between gene expression and fluctuant chromatin structural features. Therefore, we suggest that a comprehensive genome-wide structure-function relationship facilitates the comprehensive dynamical processes of muscle ontogenesis, development, and aging over time. Additional experiments are needed for the validation of muscle-related genes functioning through the formation of chromatin loops. Furthermore, networks between architecture and function could be used to probe candidate transcriptional factors mediating muscle performance in agricultural animals.

Acknowledgements

This work was supported by the National Key R & D Program of China (2023YFD1300040 and 2022YFF1000100), the Sichuan Science and Technology Program, China (2022NSFSC0132, 2021YFYZ0009 and 2022JDJQ0054), the National Natural Science Foundation of China (32225046).

Declaration of competing interest

The authors declare that they have no conflict of interest.

Declaration of generative AI and AI-assisted technologies in the writing process

The authors declare that they did not use AI in the preparation and writing of this manuscript.

Ethical approval

All experiments were conducted in compliance with the guidelines approved by the Institutional Animal Care and Use Committee of Sichuan Agricultural University, China (approval ID: 80082), and all efforts were made to minimize animal suffering.

Data availability

All data generated or analyzed during this study are included in this published article, its supplementary information files and publicly available repositories. The raw Hi-C datasets have been deposited in SRA repository under accession code “PRJNA870674”, RNA-seq datasets were available in the SRA repository under accession code “PRJNA866681”, and ChIP-seq datasets were available under accession code “PRJNA870907”.

Appendices associated with this study are available at https://doi.org/10.1016/j.jia.2024.03.052

References

Bentzinger C F, Wang Y X, Rudnicki M A. 2012. Building muscle: Molecular regulation of myogenesis. *Cold Spring Harbor Perspectives in Biology*, **4**, a008342

Berti F, Nogueira J M, Wohrle S, Sobreira D R, Hawrot K, Dietrich S. 2015. Time course and side-by-side analysis of mesodermal, pre-myogenic, myogenic and differentiated cell markers in the chicken model for skeletal muscle formation. *Journal of Anatomy*, **227**, 361–382.

Bryson-Richardson R J, Currie P D. 2008. The genetics of vertebrate myogenesis. *Nature Review in Genetics*, **9**, 632–646.

Buckingham M, Rigby P W. 2014. Gene regulatory networks and transcriptional mechanisms that control myogenesis. *Developmental Cell*, **28**, 225–238.

Cardoso-Moreira M, Halbert J, Valloton D, Velten B, Chen C, Shao Y, Liechti A, Ascencao K, Rummel C, Ovchinnikova S, Mazin P V, Xenarios I, Harshman K, Mort M, Cooper D N, Sandi C, Soares M J, Ferreira P G, Afonso S, Carneiro M, *et al.* 2019. Gene expression across mammalian organ development. *Nature*, **571**, 505–509.

Chandra T, Ewels P A, Schoenfelder S, Furlan-Magaril M, Wingett S W, Kirschner K, Thuret J Y, Andrews S, Fraser P, Reik W. 2015. Global reorganization of the nuclear landscape in senescent cells. *Cell Reports*, **10**, 471–483.

Chen G, Wang Y, Garate M, Zhou J, Li G. 2010. The tumor suppressor ING3 is degraded by SCF(Skp2)-mediated ubiquitin-proteasome system. *Oncogene*, **29**, 1498–1508.

Chen L, Li J, Yuan R, Wang Y, Zhang J, Lin Y, Wang L, Zhu X, Zhu W, Bai J, Kong F, Zeng B, Lu L, Ma J, Long K, Jin L, Huang Z, Huo J, Gu Y, Wang D, Mo D, *et al.* 2022. Dynamic 3D genome reorganization during development and metabolic stress of the porcine liver. *Cell Discovery*, **8**, 56.

Chen W, Lv Y T, Zhang H X, Ruan D, Wang S, Lin Y C. 2013. Developmental specificity in skeletal muscle of late-term avian embryos and its potential manipulation. *Poultry Science*, **92**, 2754–2764.

Chin R M, Fu X, Pai M Y, Vergnes L, Hwang H, Deng G, Diep S, Lomenick B, Meli V S, Monsalve G C, Hu E, Whelan S A, Wang J X, Jung G, Solis G M, Fazlollahi F, Kaweeteerawat C, Quach A, Nili M, Krall A S, *et al.* 2014. The metabolite alpha-ketoglutarate extends lifespan by inhibiting ATP synthase and TOR. *Nature*, **510**, 397–401.

Chung C Y T, Lo P H Y, Lee K K H. 2020. *Babam2* regulates cell cycle progression and pluripotency in mouse embryonic stem cells as revealed by induced DNA damage. *Biomedicines*, **8**, 397.

Coppe J P, Desprez P Y, Krtolica A, Campisi J. 2010. The senescence-associated secretory phenotype: The dark side of tumor suppression. *Annual Review of Pathology*, **5**, 99–118.

Courtois-Cox S, Jones S L, Cichowski K. 2008. Many roads lead to oncogene-induced senescence. *Oncogene*, **27**, 2801–2809.

Crane E, Bian Q, McCord R P, Lajoie B R, Wheeler B S, Ralston E J, Uzawa S, Dekker J, Meyer B J. 2015. Condensin-driven remodelling of X chromosome topology during dosage compensation. *Nature*, **523**, 240–244.

Criscione S W, Teo Y V, Neretti N. 2016. The chromatin landscape of

cellular senescence. *Trends in Genetics*: *TIG*, **32**, 751–761.
David V, Martin A, Hedge A M, Rowe P S. 2009. Matrix extracellular phosphoglycoprotein (MEPE) is a new bone renal hormone and vascularization modulator. *Endocrinology*, **150**, 4012–4023.
Deschamps J, Duboule D. 2017. Embryonic timing, axial stem cells, chromatin dynamics, and the Hox clock. *Genes & Development*, **31**, 1406–1416.
Dethlefsen M M, Halling J F, Moller H D, Plomgaard P, Regenberg B, Ringholm S, Pilegaard H. 2018. Regulation of apoptosis and autophagy in mouse and human skeletal muscle with aging and lifelong exercise training. *Experimental Gerontology*, **111**, 141–153.
Dittmer J. 2003. The biology of the Ets1 proto-oncogene. *Molecular Cancer*, **2**, 29.
Dixon J R, Jung I, Selvaraj S, Shen Y, Antosiewicz-Bourget J E, Lee A Y, Ye Z, Kim A, Rajagopal N, Xie W, Diao Y, Liang J, Zhao H, Lobanenkov V V, Ecker J R, Thomson J A, Ren B. 2015. Chromatin architecture reorganization during stem cell differentiation. *Nature*, **518**, 331–336.
Dixon J R, Selvaraj S, Yue F, Kim A, Li Y, Shen Y, Hu M, Liu J S, Ren B. 2012. Topological domains in mammalian genomes identified by analysis of chromatin interactions. *Nature*, **485**, 376–380.
Doi T, Puri P, Bannigan J, Thompson J. 2012. *Eya1* and *Eya2* gene expression is down-regulated during somitic myogenesis in the cadmium-induced omphalocele chick model. *Journal of Pediatric Surgery*, **47**, 1123–1127.
Durand N C, Shamim M S, Machol I, Rao S S, Huntley M H, Lander E S, Aiden E L. 2016. Juicer provides a one-click system for analyzing loop-resolution Hi-C experiments. *Cell Systems*, **3**, 95–98.
Esteves de Lima J, Bou Akar R, Mansour M, Rocancourt D, Buckingham M, Relaix F. 2021. M-Cadherin Is a *PAX3* target during myotome patterning. *Frontiers in Cell Developmental Biology*, **9**, 652652.
Fishman V, Battulin N, Nuriddinov M, Maslova A, Zlotina A, Strunov A, Chervyakova D, Korablev A, Serov O, Krasikova A. 2019. 3D organization of chicken genome demonstrates evolutionary conservation of topologically associated domains and highlights unique architecture of erythrocytes' chromatin. *Nucleic Acids Research*, **47**, 648–665.
Flyamer I M, Gassler J, Imakaev M, Brandão H B, Ulianov S V, Abdennur N, Razin S V, Mirny L A, Tachibana-Konwalski K. 2017. Single-nucleus Hi-C reveals unique chromatin reorganization at oocyte-to-zygote transition. *Nature*, **544**, 110–114.
Ghosh S, Chan C K. 2016. Analysis of RNA-seq data using TopHat and Cufflinks. *Methods in Molecular Biology*, **1374**, 339–361.
Grifone R, Demignon J, Giordani J, Niro C, Souil E, Bertin F, Laclef C, Xu P X, Maire P. 2007. Eya1 and Eya2 proteins are required for hypaxial somitic myogenesis in the mouse embryo. *Developmental Biology*, **302**, 602–616.
Grove B K, Cerny L, Perriard J C, Eppenberger H M. 1985. Myomesin and M-protein: Expression of two M-band proteins in pectoral muscle and heart during development. *The Journal of Cell Biology*, **101**, 1413–1421.
Gupta A, Place M, Goldstein S, Sarkar D, Zhou S, Potamousis K, Kim J, Flanagan C, Li Y, Newton M A, Callander N S, Hematti P, Bresnick E H, Ma J, Asimakopoulos F, Schwartz D C. 2015. Single-molecule analysis reveals widespread structural variation in multiple myeloma. *Proceedings of the National Academy of Sciences of the United States of America*, **112**, 7689–7694.
Knížetová H, Hyánek J, Hyánková L, Bělíček P. 1995. Comparative study of growth curves in poultry. *Genetics Selection Evolution*, **27**, 365–375.
Hammoud S S, Low D H P, Yi C, Carrell D T, Guccione E, Cairns B R. 2014. Chromatin and transcription transitions of mammalian adult germline stem cells and spermatogenesis. *Cell Stem Cell*, **15**, 239–253.
Heinz S, Benner C, Spann N, Bertolino E, Lin Y C, Laslo P, Cheng J X, Murre C, Singh H, Glass C K. 2010. Simple combinations of lineage-determining transcription factors prime *cis*-regulatory elements required for macrophage and B cell identities. *Molecular Cell*, **38**, 576–589.
van Hengel J, Calore M, Bauce B, Dazzo E, Mazzotti E, De Bortoli M, Lorenzon A, Li Mura I E, Beffagna G, Rigato I, Vleeschouwers M, Tyberghein K, Hulpiau P, van Hamme E, Zaglia T, Corrado D, Basso C, Thiene G, Daliento L, Nava A, *et al.* 2013. Mutations in the area composita protein alphaT-catenin are associated with arrhythmogenic right ventricular cardiomyopathy. *European Heart Journal*, **34**, 201–210.
Hernandez S F, Vahidi N A, Park S, Weitzel R P, Tisdale J, Rueda B R, Wolff E F. 2015. Characterization of extracellular DDX4- or Ddx4-positive ovarian cells. *Nature Medcine*, **21**, 1114–1116.
Huang Q, Li F, Liu X, Li W, Shi W, Liu F F, O'Sullivan B, He Z, Peng Y, Tan A C, Zhou L, Shen J, Han G, Wang X J, Thorburn J, Thorburn A, Jimeno A, Raben D, Bedford J S, Li C Y. 2011. Caspase 3-mediated stimulation of tumor cell repopulation during cancer radiotherapy. *Nature Medcine*, **17**, 860–866.
Hug C B, Vaquerizas J M. 2018. The birth of the 3D genome during early embryonic development. *Trends in Genetics*, **34**, 903–914.
Imakaev M, Fudenberg G, McCord R P, Naumova N, Goloborodko A, Lajoie B R, Dekker J, Mirny L A. 2012. Iterative correction of Hi-C data reveals hallmarks of chromosome organization. *Nature Methods*, **9**, 999–1003.
Ishihara T, Ikeda K, Sato S, Yajima H, Kawakami K. 2008. Differential expression of Eya1 and Eya2 during chick early embryonic development. *Gene Expression Patterns*, **8**, 357–367.
Janssens B, Mohapatra B, Vatta M, Goossens S, Vanpoucke G, Kools P, Montoye T, van Hengel J, Bowles N E, van Roy F, Towbin J A. 2003. Assessment of the *CTNNA3* gene encoding human alpha T-catenin regarding its involvement in dilated cardiomyopathy. *Human Genetics*, **112**, 227–236.
Jejurikar S S, Henkelman E A, Cederna P S, Marcelo C L, Urbanchek M G, Kuzon Jr W M. 2006. Aging increases the susceptibility of skeletal muscle derived satellite cells to apoptosis. *Experimental Gerontology*, **41**, 828–836.
Jin L, Wang D, Zhang J, Liu P, Wang Y, Lin Y, Liu C, Han Z, Long K, Li D, Jiang Y, Li G, Zhang Y, Bai J, Li X, Li J, Lu L, Kong F, Wang X, Li H, *et al.* 2023. Dynamic chromatin architecture of the porcine adipose tissues with weight gain and loss. *Nature Communications*, **14**, 3457.
Kalmes A, Daum G, Clowes A W. 2001. *EGFR* transactivation in the regulation of SMC function. *Annals of the New York Academy of Sciences*, **947**, 42–54.
Kim D, Pertea G, Trapnell C, Pimentel H, Kelley R, Salzberg S L. 2013. TopHat2: Accurate alignment of transcriptomes in the presence of insertions, deletions and gene fusions. *Genome Biology*, **14**, R36.
Knight P A, Ruiz D. 2012. A fast algorithm for matrix balancing. *IMA Journal of Numerical Analysis*, **33**, 1029–1047.
Kocamis H, McFarland D C, Killefer J. 2001. Temporal expression of growth factor genes during myogenesis of satellite cells derived from the biceps femoris and pectoralis major muscles of the chicken. *Journal of Cellular Physiology*, **186**, 146–152.
Kong S, Zhang Y. 2019. Deciphering Hi-C: From 3D genome to function. *Cell Biology and Toxicology*, **35**, 15–32.
Kragesteen B K, Spielmann M, Paliou C, Heinrich V, Schopflin R, Esposito A, Annunziatella C, Bianco S, Chiariello A M, Jerkovic I, Harabula I, Guckelberger P, Pechstein M, Wittler L, Chan W L, Franke M, Lupianez D G, Kraft K, Timmermann B, Vingron M, *et al.* 2018. Dynamic 3D chromatin architecture contributes to enhancer specificity and limb morphogenesis. *Nature Genetics*, **50**, 1463–1473.
Krijger P H, Di Stefano B, de Wit E, Limone F, van Oevelen C, de Laat W, Graf T. 2016. Cell-of-origin-specific 3D genome structure acquired during somatic cell reprogramming. *Cell Stem Cell*, **18**, 597–610.
Lamber E P, Guicheney P, Pinotsis N. 2022. The role of the M-band myomesin proteins in muscle integrity and cardiac disease. *Journal of Biomedical Science*, **29**, 18.
Langmead B, Salzberg S L. 2012. Fast gapped-read alignment with Bowtie 2. *Nature Methods*, **9**, 357–359.
Li C, Liu F, Liu S, Pan H, Du H, Huang J, Xie Y, Li Y, Zhao R, Wei Y. 2020. Elevated myocardial SORBS2 and the underlying implications in left ventricular noncompaction cardiomyopathy. *eBioMedicine*, **53**, 102695.
Li D, He M, Tang Q, Tian S, Zhang J, Li Y, Wang D, Jin L, Ning C, Zhu W, Hu S, Long K, Ma J, Liu J, Zhang Z, Li M. 2022a. Comparative 3D genome architecture in vertebrates. *BMC Biology*, **20**, 99.
Li D, Li Y, Li M, Che T, Tian S, Chen B, Zhou X, Zhang G, Gaur U, Luo M, Tian K, He M, He S, Xu Z, Jin L, Tang Q, Dai Y, Xu H, Hu Y, Zhao X, *et al.* 2019. Population genomics identifies patterns of genetic diversity and selection in chicken. *BMC Genomics*, **20**, 263.
Li D, Ning C, Zhang J, Wang Y, Tang Q, Kui H, Wang T, He M, Jin L, Li

J, Lin Y, Zeng B, Yin H, Zhao X, Zhang Y, Xu H, Zhu Q, Li M. 2022b. Dynamic transcriptome and chromatin architecture in granulosa cells during chicken folliculogenesis. *Nature Communications*, **13**, 131.

Li H, Cybulsky M I, Gimbrone Jr M A, Libby P. 1993. Inducible expression of vascular cell adhesion molecule-1 by vascular smooth muscle cells in vitro and within rabbit atheroma. *The American Journal of Pathology*, **143**, 1551–1559.

Li H, Durbin R. 2010. Fast and accurate long-read alignment with Burrows-Wheeler transform. *Bioinformatics*, **26**, 589–595.

Liang F, Wang B, Geng J, You G, Fa J, Zhang M, Sun H, Chen H, Fu Q, Zhang X, Zhang Z. 2021. *SORBS2* is a genetic factor contributing to cardiac malformation of 4q deletion syndrome patients. *eLife*, **10**, e67481.

Lieberman-Aiden E, van Berkum N L, Williams L, Imakaev M, Ragoczy T, Telling A, Amit I, Lajoie B R, Sabo P J, Dorschner M O, Sandstrom R, Bernstein B, Bender M A, Groudine M, Gnirke A, Stamatoyannopoulos J, Mirny L A, Lander E S, Dekker J. 2009. Comprehensive mapping of long-range interactions reveals folding principles of the human genome. *Science*, **326**, 289–293.

Liesenfeld M, Mosig S, Funke H, Jansen L, Runnebaum I B, Durst M, Backsch C. 2013. *SORBS2* and *TLR3* induce premature senescence in primary human fibroblasts and keratinocytes. *BMC Cancer*, **13**, 507.

Lindsly S, Chen C, Liu S, Ronquist S, Dilworth S, Perlman M, Rajapakse I. 2021. 4DNvestigator: Time series genomic data analysis toolbox. *Nucleus*, **12**, 58–64.

Ljt K, Rh V D W, Ketting R F, De W E. 2018. Systemic loss and gain of chromatin architecture throughout zebrafish development. *Cell Reports*, **24**, 1–10.

Lombardo S D, Mazzon E, Basile M S, Campo G, Corsico F, Presti M, Bramanti P, Mangano K, Petralia M C, Nicoletti F, Fagone P. 2019. Modulation of tetraspanin 32 (TSPAN32) expression in T cell-mediated immune responses and in multiple sclerosis. *International Journal of Molecular Sciences*, **20**, 4323.

Love M I, Huber W, Anders S. 2014. Moderated estimation of fold change and dispersion for RNA-seq data with DESeq2. *Genome Biology*, **15**, 550.

Lu H, Ju D D, Yang G D, Zhu L Y, Yang X M, Li J, Song W W, Wang J H, Zhang C C, Zhang Z G, Zhang R. 2019. Targeting cancer stem cell signature gene *SMOC-2* overcomes chemoresistance and inhibits cell proliferation of endometrial carcinoma. *eBioMedicine*, **40**, 276–289.

Luo W, Lin Z, Chen J, Chen G, Zhang S, Liu M, Li H, He D, Liang S, Luo Q, Zhang D, Nie Q, Zhang X. 2021. *TMEM182* interacts with integrin beta 1 and regulates myoblast differentiation and muscle regeneration. *Journal of Cachexia*, *Sarcopenia and Muscle*, **12**, 1704–1723.

Lupianez D G, Kraft K, Heinrich V, Krawitz P, Brancati F, Klopocki E, Horn D, Kayserili H, Opitz J M, Laxova R, Santos-Simarro F, Gilbert-Dussardier B, Wittler L, Borschiwer M, Haas S A, Osterwalder M, Franke M, Timmermann B, Hecht J, Spielmann M, *et al.* 2015. Disruptions of topological chromatin domains cause pathogenic rewiring of gene-enhancer interactions. *Cell*, **161**, 1012–1025.

MacPhillamy C, Pitchford W S, Alinejad-Rokny H, Low W Y. 2021. Opportunity to improve livestock traits using 3D genomics. *Animal Genetics*, **52**, 785–798.

Magli A, Baik J, Pota P, Cordero C O, Kwak I Y, Garry D J, Love P E, Dynlacht B D, Perlingeiro R C R. 2019. *Pax3* cooperates with *Ldb1* to direct local chromosome architecture during myogenic lineage specification. *Nature Communications*, **10**, 2316.

Maharjan P, Beitia A, Weil J, Suesuttajit N, Hilton K, Caldas J, Umberson C, Martinez D, Kong B, Owens C M, Coon C. 2021. Woody breast myopathy broiler show age-dependent adaptive differential gene expression in pectoralis major and altered *in-vivo* triglyceride kinetics in adipogenic tissues. *Poultry Science*, **100**, 101092.

Malik L, Patro R. 2019. Rich chromatin structure prediction from Hi-C data. *IEEE/ACM Transactions on Computational Biology and Bioinformatics*, **16**, 1448–1458.

Martone J, Mariani D, Desideri F, Ballarino M. 2019. Non-coding RNAs shaping muscle. *Frontiers in Cell and Developmental Biology*, **7**, 394.

Matharu N, Ahituv N. 2015. Minor loops in major folds: Enhancer-promoter looping, chromatin restructuring, and their association with transcriptional regulation and disease. *PLoS Genetics*, **11**, e1005640.

Mele M, Ferreira P G, Reverter F, DeLuca D S, Monlong J, Sammeth M, Young T R, Goldmann J M, Pervouchine D D, Sullivan T J, Johnson R, Segre A V, Djebali S, Niarchou A, Consortium G T, Wright F A, Lappalainen T, Calvo M, Getz G, Dermitzakis E T, *et al.* 2015. Human genomics. The human transcriptome across tissues and individuals. *Science*, **348**, 660–665.

Molina-Privado I, Jimenez P R, Montes-Moreno S, Chiodo Y, Rodriguez-Martinez M, Sanchez-Verde L, Iglesias T, Piris M A, Campanero M R. 2012. E2F4 plays a key role in Burkitt lymphoma tumorigenesis. *Leukemia*, **26**, 2277–2285.

Neems D S, Garza-Gongora A G, Smith E D, Kosak S T. 2016. Topologically associated domains enriched for lineage-specific genes reveal expression-dependent nuclear topologies during myogenesis. *Proceedings of the National Academy of Sciences of the United States of America*, **113**, E1691–E1700.

Newman A B, Kupelian V, Visser M, Simonsick E M, Goodpaster B H, Kritchevsky S B, Tylavsky F A, Rubin S M, Harris T B, Ofhealth, Behalf O. 2006. Strength, but not muscle mass, is associated with mortality in the health, aging and body composition study cohort. *The Journals of Gerontology Series A* (Biological Sciences and Medical Sciences), **61**, 72–77.

Nkabyo Y S, Go Y M, Ziegler T R, Jones D P. 2005. Extracellular cysteine/cystine redox regulates the p44/p42 MAPK pathway by metalloproteinase-dependent epidermal growth factor receptor signaling. *American Journal of Physiology Gastrointestinal and Liver Physiology*, **289**, G70–G78.

Noordermeer D, Leleu M, Schorderet P, Joye E, Chabaud F, Duboule D. 2014. Temporal dynamics and developmental memory of 3D chromatin architecture at Hox gene loci. *eLife*, **3**, e02557.

Nora E P, Lajoie B R, Schulz E G, Giorgetti L, Okamoto I, Servant N, Piolot T, van Berkum N L, Meisig J, Sedat J, Gribnau J, Barillot E, Bluthgen N, Dekker J, Heard E. 2012. Spatial partitioning of the regulatory landscape of the X-inactivation centre. *Nature*, **485**, 381–385.

Nueda M J, Tarazona S, Conesa A. 2014. Next maSigPro: Updating maSigPro bioconductor package for RNA-seq time series. *Bioinformatics*, **30**, 2598–2602.

Paliou C, Guckelberger P, Schopflin R, Heinrich V, Esposito A, Chiariello A M, Bianco S, Annunziatella C, Helmuth J, Haas S, Jerkovic I, Brieske N, Wittler L, Timmermann B, Nicodemi M, Vingron M, Mundlos S, Andrey G. 2019. Preformed chromatin topology assists transcriptional robustness of *Shh* during limb development. *Proceedings of the National Academy of Sciences of the United States of America*, **116**, 12390–12399.

Pan W, Zhang N, Liu W, Liu J, Zhou L, Liu Y, Yang M. 2018. The long noncoding RNA GAS8-AS1 suppresses hepatocarcinogenesis by epigenetically activating the tumor suppressor GAS8. *The Journal of Biological Chemistry*, **293**, 17154–17165.

Parker M H, Seale P, Rudnicki M A. 2003. Looking back to the embryo: Defining transcriptional networks in adult myogenesis. *Nature Reviews Genetics*, **4**, 497–507.

Paulsen J, Liyakat Ali T M, Nekrasov M, Delbarre E, Baudement M O, Kurscheid S, Tremethick D, Collas P. 2019. Long-range interactions between topologically associating domains shape the four-dimensional genome during differentiation. *Nature Genetics*, **51**, 835–843.

Pertea M, Pertea G M, Antonescu C M, Chang T C, Mendell J T, Salzberg S L. 2015. StringTie enables improved reconstruction of a transcriptome from RNA-seq reads. *Nature Biotechnology*, **33**, 290–295.

Prenzel N, Fischer O M, Streit S, Hart S, Ullrich A. 2001. The epidermal growth factor receptor family as a central element for cellular signal transduction and diversification. *Endocrine Related Cancer*, **8**, 11–31.

Quiat D, Voelker K A, Pei J, Grishin N V, Grange R W, Bassel-Duby R, Olson E N. 2011. Concerted regulation of myofiber-specific gene expression and muscle performance by the transcriptional repressor Sox6. *Proceedings of the National Academy of Sciences of the United States of America*, **108**, 10196–10201.

Rao S S, Huntley M H, Durand N C, Stamenova E K, Bochkov I D, Robinson J T, Sanborn A L, Machol I, Omer A D, Lander E S,

Aiden E L. 2014. A 3D map of the human genome at kilobase resolution reveals principles of chromatin looping. *Cell*, **159**, 1665–1680.
Rieber L, Mahony S. 2017. miniMDS: 3D structural inference from high-resolution Hi-C data. *Bioinformatics*, **33**, i261-i266.
Robin J D, Jacome Burbano M S, Peng H, Croce O, Thomas J L, Laberthonniere C, Renault V, Lototska L, Pousse M, Tessier F, Bauwens S, Leong W, Sacconi S, Schaeffer L, Magdinier F, Ye J, Gilson E. 2020. Mitochondrial function in skeletal myofibers is controlled by a TRF2-SIRT3 axis over lifetime. *Aging Cell*, **19**, e13097.
Rosa-Garrido M, Chapski D J, Schmitt A D, Kimball T H, Karbassi E, Monte E, Balderas E, Pellegrini M, Shih T T, Soehalim E, Liem D, Ping P, Galjart N J, Ren S, Wang Y, Ren B, Vondriska T M. 2017. High-resolution mapping of chromatin conformation in cardiac myocytes reveals structural remodeling of the epigenome in heart failure. *Circulation*, **136**, 1613–1625.
Rowley M J, Nichols M H, Lyu X, Ando-Kuri M, Rivera I S M, Hermetz K, Wang P, Ruan Y, Corces V G. 2017. Evolutionarily conserved principlespredict 3D chromatin organization. *Molecular Cell*, **67**, 837–852.e7.
Ruis P, Van Ly D, Borel V, Kafer G R, McCarthy A, Howell S, Blassberg R, Snijders A P, Briscoe J, Niakan K K, Marzec P, Cesare A J, Boulton S J. 2021. TRF2-independent chromosome end protection during pluripotency. *Nature*, **589**, 103–109.
Salama R, Sadaie M, Hoare M, Narita M. 2014. Cellular senescence and its effector programs. *Genes & Development*, **28**, 99–114.
Sanders S J, Campbell A J, Cottrell J R, Moller R S, Wagner F F, Auldridge A L, Bernier R A, Catterall W A, Chung W K, Empfield J R, George Jr A L, Hipp J F, Khwaja O, Kiskinis E, Lal D, Malhotra D, Millichap J J, Otis T S, Petrou S, Pitt G, *et al.* 2018. Progress in understanding and treating SCN2A-mediated disorders. *Trends in Neuroscience*, **41**, 442–456.
Sati S, Bonev B, Szabo Q, Jost D, Bensadoun P, Serra F, Loubiere V, Papadopoulos G L, Rivera-Mulia J C, Fritsch L, Bouret P, Castillo D, Gelpi J L, Orozco M, Vaillant C, Pellestor F, Bantignies F, Marti-Renom M A, Gilbert D M, Lemaitre J M, *et al.* 2020. 4D Genome rewiring during oncogene-induced and replicative senescence. *Molecular Cell*, **78**, 522–538. e9.
Schrauwen I, Valgaeren H, Tomas-Roca L, Sommen M, Altunoglu U, Wesdorp M, Beyens M, Fransen E, Nasir A, Vandeweyer G, Schepers A, Rahmoun M, van Beusekom E, Huentelman M J, Offeciers E, Dhooghe I, Huber A, Van de Heyning P, Zanetti D, De Leenheer E M R, *et al.* 2019. Variants affecting diverse domains of MEPE are associated with two distinct bone disorders, a craniofacial bone defect and otosclerosis. *Genetics in Medcine*, **21**, 1199–1208.
Sousa-Victor P, Garcia-Prat L, Munoz-Canoves P. 2022. Control of satellite cell function in muscle regeneration and its disruption in ageing. *Nature Reviews*. *Molecular Cell Biology*, **23**, 204–226.
Stanic B, Katsuyama M, Miller Jr F J. 2010. An oxidized extracellular oxidation-reduction state increases Nox1 expression and proliferation in vascular smooth muscle cells *via* epidermal growth factor receptor activation. *Arteriosclerosis*, *Thrombosis*, *and Vascular Biology*, **30**, 2234–2241.
Su Y, Wang T, Wu N, Li D, Fan X, Xu Z, Mishra S K, Yang M. 2019. Alpha-ketoglutarate extends *Drosophila* lifespan by inhibiting mTOR and activating AMPK. *Aging*, **11**, 4183–4197.
Surakka I, Fritsche L G, Zhou W, Backman J, Kosmicki J A, Lu H, Brumpton B, Nielsen J B, Gabrielsen M E, Skogholt A H, Wolford B, Graham S E, Chen Y E, Lee S, Kang H M, Langhammer A, Forsmo S, Asvold B O, Styrkarsdottir U, Holm H, Gudbjartsson D, *et al.* 2020. MEPE loss-of-function variant associates with decreased bone mineral density and increased fracture risk. *Nature Communications*, **11**, 4093.
Syafruddin S E, Mohtar M A, Wan Mohamad Nazarie W F, Low T Y. 2020. Two sides of the same coin: The roles of *KLF6* in physiology and pathophysiology. *Biomolecules*, **10**, 1378.
Symmons O, Pan L, Remeseiro S, Aktas T, Klein F, Huber W, Spitz F. 2016. The *Shh* topological domain facilitates the action of remote enhancers by reducing the effects of genomic distances. *Developmental Cell*, **39**, 529–543.
Taglietti V, Maroli G, Cermenati S, Monteverde S, Ferrante A, Rossi G, Cossu G, Beltrame M, Messina G. 2016. Nfix induces a switch in *Sox6* transcriptional activity to regulate MyHC-I expression in fetal muscle. *Cell Reports*, **17**, 2354–2366.
Tiscia G L, Margaglione M. 2018. Human fibrinogen: Molecular and genetic aspects of congenital disorders. *International Journal of Molecular Sciences*, **19**, 1597.
Whyte W A, Orlando D A, Hnisz D, Abraham B J, Lin C Y, Kagey M H, Rahl P B, Lee T I, Young R A. 2013. Master transcription factors and mediator establish super-enhancers at key cell identity genes. *Cell*, **153**, 307–319.
Williams T M, Lisanti M P. 2004. The caveolin proteins. *Genome Biology*, **5**, 214.
Xu P X, Cheng J, Epstein J A, Maas R L. 1997. Mouse *Eya* genes are expressed during limb tendon development and encode a transcriptional activation function. *Proceedings of the National Academy of Sciences of the United States of America*, **94**, 11974–11979.
Xu Z, Che T, Li F, Tian K, Zhu Q, Mishra S K, Dai Y, Li M, Li D. 2018. The temporal expression patterns of brain transcriptome during chicken development and ageing. *BMC Genomics*, **19**, 917.
Yang T, Zhang F, Yardimci G G, Song F, Hardison R C, Noble W S, Yue F, Li Q. 2017. HiCRep: Assessing the reproducibility of Hi-C data using a stratum-adjusted correlation coefficient. *Genome Research*, **27**, 1939–1949.
Yau M S, Kuipers A L, Price R, Nicolas A, Tajuddin S M, Handelman S K, Arbeeva L, Chesi A, Hsu Y H, Liu C T, Karasik D, Zemel B S, Grant S F, Jordan J M, Jackson R D, Evans M K, Harris T B, Zmuda J M, Kiel D P. 2021. A meta-analysis of the transferability of bone mineral density genetic loci associations from European to African ancestry populations. *Journal of Bone and Mineral Research*, **36**, 469–479.
Yuan R, Zhang J, Wang Y, Zhu X, Hu S, Zeng J, Liang F, Tang Q, Chen Y, Chen L, Zhu W, Li M, Mo D. 2021. Reorganization of chromatin architecture during prenatal development of porcine skeletal muscle. *DNA Research*, **28**, 1–11.
Zhan Y, Mariani L, Barozzi I, Schulz E G, Bluthgen N, Stadler M, Tiana G, Giorgetti L. 2017. Reciprocal insulation analysis of Hi-C data shows that TADs represent a functionally but not structurally privileged scale in the hierarchical folding of chromosomes. *Genome Research*, **27**, 479–490.
Zhang Y, Liu T, Meyer C A, Eeckhoute J, Johnson D S, Bernstein B E, Nusbaum C, Myers R M, Brown M, Li W, Liu X S. 2008. Model-based analysis of ChIP-seq (MACS). *Genome Biology*, **9**, R137.
Zheng H, Xie W. 2019. The role of 3D genome organization in development and cell differentiation. *Nature Reviews*. *Molecular Cell Biology*, **20**, 53tt50.
Zhou Y, Zhou B, Pache L, Chang M, Khodabakhshi A H, Tanaseichuk O, Benner C, Chanda S K. 2019. Metascape provides a biologist-oriented resource for the analysis of systems-level datasets. *Nature Communications*, **10**, 1523.
Zhu B, Rippe C, Holmberg J, Zeng S, Perisic L, Albinsson S, Hedin U, Uvelius B, Swärd K. 2018. Nexilin/NEXN controls actin polymerization in smooth muscle and is regulated by myocardin family coactivators and YAP. *Scientific Reports*, **8**, 13025.

Executive Editor-in-Chief Kui LI
Managing Editor Han Zhang